UiO : Department of Geosciences
University of Oslo

Greenland Surface Energy Budget response in CMIP6

Idunn Aamnes Mostue

Master's Thesis, Spring 2022

Abstract

The Greenland Ice Sheet (GrIS) has been losing mass since the 1990s as a direct consequence of rising temperatures. Greenland has been projected to continue to lose mass at an accelerating pace throughout the 21st century, making it one of the the largest contributors to future sea-level rise. The latest Climate Model Intercomparison Project 6th phase (CMIP6) models produce a greater Arctic amplification signal and therefore also a notably larger mass loss from the GrIS when compared to the older CMIP5 projections, despite similar forcing levels from greenhouse gas emissions. However, it is also argued that the strength of regional factors such as melt-albedo feedbacks and cloud-related feedbacks will partly impact future melt and sea-level rise contribution, but little is yet known about the role of these regional factors in future GrIS surface melt projections when comparing CMIP6 to CMIP5 over Greenland. In this study, we use high-resolution (15 km) simulations over the GrIS performed by using the regional climate model Modéle Atmosphériqe Régional (MAR) to physically downscale six CMIP5 RCP8.5 models and five CMIP6 SSP5-8.5 models. Here, we show a greater annual mass loss from the GrIS, both at the end of the 21st century, but also for a given temperature increase over the GrIS when comparing CMIP6 to CMIP5. We find a greater sensitivity of Greenland surface mass loss in CMIP6 centred around summer and autumn, yet the difference in mass loss is largest during autumn with a reduction of 14.1 $\pm$ 4.8 mmWE for a regional warming of +6.7°C, 12.5 mmWE more mass loss than in CMIP5 RCP8.5 simulations. Assessment of the surface energy budget and cloud-related feedbacks suggests a reduction in high clouds during summer and autumn – in addition to enhanced cloud optical depth during autumn – to be the main drivers of the additional energy reaching the surface, subsequently leading to enhanced surface melt and mass loss in CMIP6 SSP5-8.5 compared to CMIP5 RCP8.5. Our analysis highlights that Greenland is losing more mass in CMIP6 due to two factors; 1) a (known) greater sensitivity to greenhouse gas emissions and therefore warmer temperatures, 2) previously undocumented cloud-related surface energy budget changes that enhance the GrIS sensitivity to warming.

Acknowledgements

First and foremost, I would like to thank my two supervisors Stefan Hofer and Trude Storelvmo, for their availability, constructive feedback and engagement. Trude, thank you for taking me on board and including me in your research group, for providing opportunities for me to grow as a researcher, and for your encouragement along the way. Stefan, thank you for introducing me to the field of Greenland, for your thorough and solid academic guidance, for challenging me and building my confidence, and for your optimism and patience along the way. Without you, writing this thesis would never have been possible.

I gratefully acknowledge Xavier Fettweis, for providing me with the MAR data I have used for this thesis, and for valuable discussions and feedback. Furthermore, I am grateful for the community at MetOS for providing an open and encouraging space for master's student to contribute and evolve.

A special thank-you goes out to my master's-family at Lesesal 2418B, for their emotional support, encouragement, conversations and laughs, and for always joining in on my Friday dances. You have made me realise that getting trough a master's is about more than putting words to paper in a thesis. The supporting community and friendships we have built over the past 1.5 years is truly special and I will forever be grateful for the time we have had together.

Lastly, I would like to thank my family for their unconditional support, and for showing interest in my work. And to Sondre, for believing in my abilities, for cheering me on through all the ups and downs, and for keeping me grounded. Because of you, I have had the courage and stamina to hold on to my academic goals and never given up on reaching them.

Idunn Aamnes Mostue
January 2022
Oslo

Contents

Abstract i

Acknowledgements iii

Contents v

List of Figures vii

List of Tables ix

Abbreviations xi

1 Introduction 1
- 1.1 Motivation . . . 1
- 1.2 Research question . . . 2
- 1.3 Outline . . . 3

2 Theory and Background 5
- 2.1 Mass Budget over the Greenland Ice Sheet . . . 5
- 2.2 Driving mechanisms of recent GrIS SMB change . . . 7
- 2.3 Future projection of GrIS SMB change . . . 9

3 Methods 11
- 3.1 Research design . . . 11
- 3.2 Regional Climate Modelling . . . 12
- 3.3 MAR forcings . . . 14
- 3.4 Computation of anomalies . . . 15
- 3.5 Statistical significance . . . 16

4 Results 19
- 4.1 GrIS Surface Mass Balance change . . . 19
- 4.2 Cloud contribution to Surface Energy Budget change . . . 22
- 4.3 Spatial distribution over the GrIS . . . 25
- 4.4 Melt-albedo feedback response . . . 29

5 Discussion 33
- 5.1 Cloud induced SMB change in CMIP6 . . . 33
- 5.2 Change in cloud representation over Greenland . . . 34
- 5.3 Limitations . . . 35

6 Conclusion 37
- 6.1 Summary . . . 37

6.2 Further research 37

Appendices **39**

A Figures **41**

B Tables **51**

C Computer Code **53**

Bibliography **55**

List of Figures

1.1 Twelve-year average Surface Mass Balance over the GrIS 1

3.1 Integration domain and surface height over Greenland from MAR simulations 12
3.2 Individual model projections of near-surface temperature (averaged mean) 17

4.1 Annual and seasonal SMB, melt and runoff anomalies according to near-surface temperature anomalies 21
4.2 Radiative SEB component anomalies and cloud cover anomalies as a function of the near-surface air temperature anomalies 23
4.3 COD according to near-surface temperature 24
4.4 Spatial projection of cloud cover 26
4.5 Spatial projection of difference in anomaly of SEB fluxes between MAR CMIP6 and MAR CMIP5 simulations (+ 4°C ± 10 years) for summer and autumn. 27
4.6 Spatial projection of difference in anomaly of selected SMB components between MAR CMIP6 and MAR CMIP5 simulations (+ 4°C ± 10 years) for summer and autumn . . 29
4.7 Albedo anomalies according to the near-surface air temperature anomalies 31
4.8 Annual cycle of Albedo and SMB 32

A.1 Winter SMB, melt and runoff anomalies according to near-surface temperature anomalies 41
A.2 Spring SMB, melt and runoff anomalies according to near-surface temperature anomalies 42
A.3 Seasonal heat flux anomalies according to near-surface temperature anomalies 43
A.4 Spatial projection of summer lower-, mid-, upper- and total Cloud Cover anomalies . . 44
A.5 Spatial projection of autumn lower-, mid-, upper- and total Cloud Cover anomalies . . 45
A.6 Summer specific humidity anomalies according to near-surface temperature anomalies 46
A.7 Autumn specific humidity anomalies according to near-surface temperature anomalies 47
A.8 Annual cycle of cloud cover 48
A.9 Annual cycle of COD 49

List of Tables

3.1 MAR Greenland setup 14
3.2 Forcing fields, scenarios and CMIP phase of MAR simulations 14

4.1 Overview of projected climate variable anomalies 20

B.1 Climate variable overview 51
B.2 Regression function and R^2 score 52

Abbreviations

AR Assessment Report
CMIP Coupled Model Intercomparison Project
COD Cloud Optical Depth
GCMs Global Climate Models
GHG greenhouse gas
GrIS Greenland Ice Sheet
IPCC Intergovernmental Panel on Climate Change
ISMIP Ice Sheet Model Intercomparison Project
MAR Modéle Atmosphériqe Régional
RCMs Regional Climate Models
RCP Representative Concentration Pathways
SEB Surface Energy Budget
SMB Surface Mass Balance
SSP Shared Socio-economic Pathways

CHAPTER 1

Introduction

1.1 Motivation

The Greenland Ice Sheet (GrIS) has been losing mass at an accelerating pace since the mid-1990s, and is expected to lose mass until the end of the 21st century. Future climate projections indicate that the GrIS will be one of the largest contributors to 21st century sea-level rise, mostly due to an increase in meltwater runoff, threatening coastal human habitat and livelihood (Fettweis et al., 2013a; Doblas-Reyes et al., 2021).

Fluctuations in the mass balance of the GrIS occur with variations in meltwater runoff, glacial discharge (i.e. mass flux into the ocean), and accumulation of snow on the ice sheet surface. Recent mass loss is dominated by the reduction in Surface Mass Balance (SMB) from surface melt and subsequent runoff, with about ∼50% of the mass loss in the period between 1992–2018 coming from a decrease in SMB (The IMBIE Team, 2020). Conversely, accumulation from snowfall remained close to constant during this period (Tedesco et al., 2020). Because only a small fraction of the GrIS outlet glaciers are marine terminating, the role of a changing ocean circulation and warming

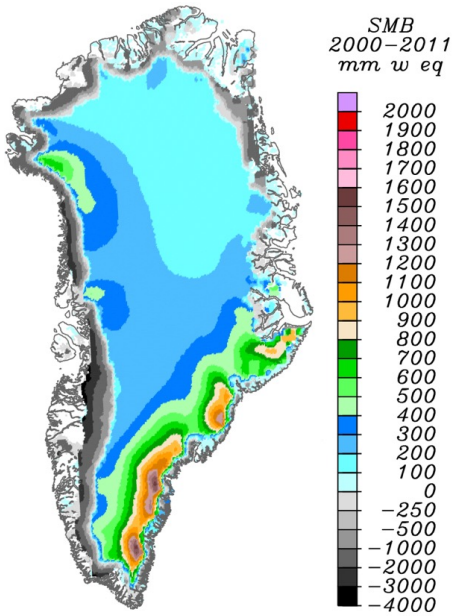

Figure 1.1: Twelve-year average Surface Mass Balance over the GrIS. (2000–2011) average Surface Mass Balance over the Greenland Ice Sheet (GrIS) according to the regional climate model simulation produced by Modéle Atmosphériqe Régional (MAR). The ablation area is indicated by grey tones, and the accumulation zone by coloured tones. Reprinted from (Box et al., 2012, p.825).

is limited. Therefore, atmospheric processes will be the dominant drivers of GrIS mass loss in the future and will also control the underlying uncertainties.

The surface melt over the GrIS occurs mostly along the edges of the ice sheet. This narrow band is called the ablation zone, and expands from just a few kilometres in the east, up to 100 km on the south-west edge of the ice sheet (see Figure 1.1). Over the ablation area the annual surface melt and meltwater runoff exceeds the accumulation of snow on the ground. Due to the dark exposed bare ice, melt in the ablation zone is mainly driven by absorbed solar radiation (Box et al., 2012; Noël et al., 2019; Broeke et al., 2008a; van den Broeke et al., 2017).

Global temperatures since the pre-industrial era have increased as a direct consequence of larger greenhouse gas (GHG) concentration in the atmosphere from anthropogenic emissions. Conversely, global observations show larger increases of the near-surface temperature over polar regions compared to the global mean. This phenomena is referred to as Arctic amplification over northern high latitudes (Goosse et al., 2018).

Arctic amplification and circulation changes over Greenland have been pointed out as the main drivers of the recent SMB loss from the GrIS. While Arctic amplification leads to an anomalous increase in the near-surface temperatures (Screen et al., 2010), more frequent anticyclonic circulation conditions lead to a reduction in clouds (Hofer et al., 2017), and enhanced melt-albedo feedback (Box et al., 2012). However, in future projections the underlying physical mechanisms driving the SMB reduction through surface melt and runoff constitute some of the main uncertainties related to mass loss, and subsequent contribution to sea-level rise, from the GrIS in a warming climate (Hofer et al., 2017; van den Broeke et al., 2017).

The latest Coupled Model Intercomparison Project (CMIP) 6^{th} phase models produce a greater Arctic amplification signal and therefore also a notably larger mass loss from the GrIS when compared to older CMIP5 projections, despite using nominally comparable forcing scenarios (O'Neill et al., 2016). However, the strength of regional factors such as melt-albedo feedbacks and cloud-related feedbacks will partly impact future melt and sea-level rise contribution by altering the energy available for melt at the surface. Yet, little is known about the role of these regional factors in future GrIS surface melt projections when comparing CMIP6 to CMIP5 over Greenland.

One way to explore the underlying physical mechanisms of future SMB reduction over the GrIS is through Regional Climate Models (RCMs). As most of the increase in melt occurs in the narrow ablation zone or through an expansion of the ablation zone, the model used to project future changes in SMB must be able to represent the dynamics at the local spatial scale of this area. By downscaling global climate models to higher spatial resolution, polar-oriented RCMs are considered the best approach to project changes in the near-surface climate and the surface-atmosphere interaction over Greenland (Fettweis et al., 2020).

1.2 Research question

Motivated by the larger mass loss from the GrIS projected by CMIP6 models compared to CMIP5 models, we want to explore the underlying physical mechanisms driving this difference. We then raise the following question:

- **With future temperature increase, does the larger reduction in SMB projected in CMIP6 come from more warming or can it be partly attributed to greater sensitivity in other underlying mechanisms?**

In this thesis we analyse regional climate model outputs with the main focus on comparing future projections at a given warming level. In this way we can disentangle whether the differences in melt and mass loss come from a greater response at a given temperature or just from the fact that CMIP6 models warm more in absolute terms over Greenland and the Arctic.

1.3 Outline

The thesis proceeds in six chapters. In Chapter 2, we provide the theoretical background and an overview of current knowledge on recent mass loss and future projections of the SMB over the GrIS. In Chapter 3, we outline the research design and give a description of the regional model setup and the calculation of anomalies and statistical significance from output data. In Chapter 4, we present the main results of our analysis. In Chapter 5, we provide a discussion on our main findings and reflect on some of the limitations of our study. In Chapter 6, we provide a summary of our main findings and contributions of our work as well as suggestions for future work.

Additionally, there are three appendices where we provide supplementary figures in Appendix A, supplementary tables in Appendix B, and description for accessing all computational code produced for the analysis of the thesis in Appendix C.

CHAPTER 2

Theory and Background

Between 1960 and the 1990s the GrIS was close to a stable state and in equilibrium with the climate system (van den Broeke et al., 2016). However, between 1992–2018 the ice sheet has transitioned to a phase of sustained mass loss, reaching 3,902 ± 342 billion tonnes, where approximately half of this mass loss happened during the six-year period from 2006–2012 alone (The IMBIE Team, 2020). When mass leaves the GrIS into the ocean – as meltwater or through iceberg calving – it contributes to global sea-level rise. It has been estimated that the GrIS holds enough water for a sea-level rise contribution of 7.42 ± 0.05 m (Morlighem et al., 2017). The GrIS is loosing mass mainly through glacial discharge, i.e. ice mass flux into the ocean, and through a reduction in SMB, i.e. more meltwater runoff from the ice sheet in melt season than what is accumulated between autumn and spring. However, the recent mass loss from the GrIS is dominated by an increase in surface melt and runoff (van den Broeke et al., 2016; Enderlin et al., 2014).

This chapter provides the theoretical basis on the SMB over the GrIS on which this study is founded in Section 2.1. Then, in Section 2.2 we give an overview of the background of the current knowledge and previous studies on the development and processes leading to the recent mass loss from the GrIS, before we look into future projections of GrIS SMB change in Section 2.3.

2.1 Mass Budget over the Greenland Ice Sheet

The recent decrease in SMB has become the dominant contributor to mass loss from the GrIS, surpassing ice discharge from marine terminating glaciers (van den Broeke et al., 2016). We can determine the SMB and its relation to the total mass balance through the following three budgets (van den Broeke et al., 2009);

First, the total ice sheet mass balance (MB, Equation (2.1)) defines the temporal changes of the overall ice sheet mass balance, through the difference in SMB and discharge (D) into the ocean (i.e. iceberg calving at the glacial outlets). However, the focus of this thesis is on the changes in mass balance coming from SMB change, thus discharge mechanisms will not be further discussed.

$$\mathrm{MB} = \frac{\mathrm{dM}}{\mathrm{dt}} = \mathrm{SMB} - \mathrm{D} \quad [\mathrm{Gt\ yr^{-}}] \tag{2.1}$$

Second, the surface mass balance (Equation (2.2)) is defined as the difference in accumulation and ablation at the surface of the ice sheet. The ice sheet gains mass through precipitation (PR) of rain and snow, and loses mass through sublimation (SU), erosion of snow by the wind (E), and meltwater runoff (RU).

$$\mathrm{SMB} = \mathrm{PR} - \mathrm{SU} - \mathrm{E} - \mathrm{RU} \quad [\mathrm{Gt\ yr^{-}}] \tag{2.2}$$

Third, the liquid water balance describes the difference in sources and sinks of liquid water, which determines the runoff (Equation (2.3)) from the SMB. Rainfall (RF), melt (ME) and water vapour condensation (CO), represent the sources, whereas refreezing (RZ) and capillary retention (CR) represent the sinks.

$$\mathrm{RU} = \mathrm{ME} + \mathrm{RF} + \mathrm{CO} - \mathrm{RZ} - \mathrm{CR} \quad [\mathrm{Gt\ yr}^{-}] \tag{2.3}$$

Meltwater can leave the ice sheet by running off at the surface, but it can also take other pathways by percolating into the snowpack and either be stored as liquid or refreeze (RZ) as ice, or collect as meltwater lakes over the ice sheet surface. For surface melt to occur in the first place the surface temperature must reach the melting point of 0°C, while excess energy is available (Lenaerts et al., 2019). Thus, we must include a fourth equation to assess the available surface energy for surface mass change.

Surface energy budget

The Surface Energy Budget (SEB) is a measure of the total energy budget of ingoing and outgoing energy fluxes over the GrIS. It determines the energy available at the surface for melt or warming of the surface or snowpack.

We are interested in the different physical processes of the SEB, and their possible contribution to the larger decrease in SMB in CMIP6 compared to CMIP5. Therefore, we proceed with a partitioning of SEB into components of different energy fluxes. First, we distinguish between radiative and non-radiative energy fluxes. The latter include the latent heat flux (LHF, i.e. the energy flux that occurs between the surface and the atmosphere when water either condenses/deposits onto or evaporates/sublimates off of the surface), the sensible heat flux (SHF, i.e the flux between the ice sheet surface and the atmosphere due to heat conduction), and the subsurface conductive heat flux (G_s).

In turn, depending on the direction of the energy flux away upwards from (U) or down towards the surface (D), and whether the wavelength is in the longwave (LW) or shortwave (SW) range of the radiation energy spectrum, we can further subdivide the radiative energy fluxes.

If we define positive direction of energy flux towards the surface, we can combine the SEB components into Equation (2.4), where SMB > 0 would mean a surplus of energy over the surface allowing melt.

$$\begin{aligned} \mathrm{SEB} &= \mathrm{LWD} - \mathrm{LWU} + \mathrm{SWD} - \mathrm{SWU} + \mathrm{SHF} + \mathrm{LHF} + \mathrm{G}_s \quad [\mathrm{Wm}^{-2}] \\ \mathrm{SEB} &= \mathrm{LWD} - (\epsilon \times \sigma \times T^4) + (\mathrm{SWD} \times (1-\alpha)) + \mathrm{SHF} + \mathrm{LHF} + \mathrm{G}_s \quad [\mathrm{Wm}^{-2}] \end{aligned} \tag{2.4}$$

The LW radiation emitted from the surface (LWU) can be represented through the thermal emissivity of the surface (ϵ), the Stefan-Boltzman constant ($\sigma = 5.67 \times 10^{-8}[\mathrm{Wm}^{-2}\mathrm{K}^{-4}]$), and the absolute temperature emitting from the surface (T). By definition, ϵ is the ratio of emitted LW radiation from a surface to that of a perfect blackbody. As we commonly consider Earth as a blackbody, the thermal emissivity is set to $\epsilon = 1$ (Marshall et al., 2007,p.14-16). We then see from Equation (2.4) that a change in LWU will only depend on a change in surface temperature.

The total or net SW radiation (SWD$\times$ (1-α)) is defined as the downward SW energy flux (SWD, i.e. incoming solar radiation) that is absorbed by the surface. This magnitude depends on the incoming solar radiation at the-top-of-the-atmosphere, the surface albedo (α, i.e. a measure of how much SW is reflected by the surface), as well as the influence of clouds, aerosols etc. on the transmissivity of the atmosphere (i.e altering the amount of SWD reaching the surface).

In turn, the presence or absence of snow over the ice sheet contributes to surface albedo variability, thus have a direct impact on the amount of absorbed SW radiation. The albedo ranges from

over 0.85 for freshly accumulated snow, to 0.7 for wet snow, and 0.55 for bare ice glacier, free of impurities. In the presence of soot, algae or other impurities accumulating on the bare ice, the albedo can drop down to values below 0.2, enhancing further absorption of SW radiation (van den Broeke et al., 2017).

Spatial and seasonal variation in SEB and SMB

The SEB, and therefore also the SMB, is not uniformly distributed over the GrIS neither spatially nor in time. The ice sheet can be divided into two zones, depending on whether it is experiencing a loss or gain in mass on an annual basis.

First, the interior of the GrIS, known as the accumulation zone, is characterised by a thick layer of multiyear-snow called "firn" (van den Broeke et al., 2017). In this area the ice sheet experiences more precipitation accumulating on the ground than what is lost through surface melt and meltwater runoff on an annual basis. The firn layer can also act as a buffer for any meltwater produced, by storing it as liquid or refreezing the meltwater. Upon freezing, latent heat is released through phase change which in turn will heat up the snowpack. The snowpack is highly reflective to most of the incoming solar radiation (i.e it has a high albedo), and so any variation in the absorbed energy budget over the accumulation zone is primarily controlled by the LW radiation fluxes (see Equation (2.4)).

Second, around the edge of the ice sheet spans a narrow area where the ice sheet experiences more surface melt and meltwater runoff than what is accumulated annually. This zone is referred to as the ablation zone. In contrast to the high albedo over the accumulation zone, the ablation zone experiences bare ice exposure during the summer melt, thus absorption of incoming solar radiation (SWD) is enhanced. Hence, in this area the energy budget is primarily controlled by SW radiation fluxes when bare ice is exposed during summer melt season.

Due to the geographical position of Greenland, the ice sheet experiences little to no incoming solar radiation for large parts of the year. The timing of the melt season is closely connected to the seasonal changes in solar radiation, where most of the surface melt occurs over the three summer months June, July and August (JJA) (Fettweis et al., 2011). The beginning of the melt season can be defined as the first day of a period of minimum three days of continuous melt of more than five percent of the ice sheet (Fettweis et al., 2005). It usually occurs in early to mid-June, and the surface melt is spatially concentrated over the ablation zone, where the surface melt variability is dominated by the amount of SW energy that is absorbed (Box et al., 2012; van den Broeke et al., 2008b). The melt season ends by mid-September, and at this time the bare ice in the ablation zone gets covered by a fresh layer of snow (Fettweis et al., 2011; Fettweis et al., 2005).

2.2 Driving mechanisms of recent GrIS SMB change

To understand what processes may be important in future SMB loss from the GrIS we need to assess the present knowledge on the recent SMB change. Across the scientific literature and through various measurement techniques (i.e. in-situ and satellite observations and model simulations) different mechanisms have been proposed as drivers of the recent surface mass loss over the GrIS. However, increasing temperatures and decreasing surface albedo due to the melt-albedo feedback have been stated as the main contributors to recent decrease in SMB from the GrIS (van den Broeke et al., 2016). Furthermore, for this thesis we want to have the main focus on the radiative energy fluxes, as these are the most important source of surface melt energy (Broeke et al., 2008a).

Atmospheric Circulation

Changes in the summer near-surface temperature is caused by changes in the local surface energy balance (e.g. radiative heat exchange, vertical mixing in the boundary layer of the atmosphere) as well as variability in atmospheric circulation over the ice sheet potentially advecting warmer air

masses (van den Broeke et al., 2017). Hanna et al., 2012 observed a significant coastal summer warming of ∼1.7°C between 1991–2019. Over the last two decades observations show circulation changes favouring anomalously warmer and drier summers over the GrIS, reducing the cloud cover (Hofer et al., 2017), and enhancing the melt through melt-albedo feedback (Fettweis et al., 2013b; Delhasse et al., 2018). Fettweis et al., 2013b estimate that 70% of the recent summer warming can be explained by an increased transport of warm air over the western part of Greenland coming from an anomalously negative North Atlantic Oscillation (NAO). However, while anomalous high-pressure conditions have been observed over Greenland in summer over the last two decades, none of the most recent state-of-the-art Global Climate Models (GCMs) (i.e. CMIP5 and CMIP6 models) have been shown to capture these circulation changes (Hanna et al., 2018;Delhasse et al., 2021).

Clouds, radiation and albedo

From the SEB (see Equation (2.4)) we know that excess amount of energy is needed in order to enable melt at the surface of the GrIS. Clouds are of first order importance in altering the GrIS energy budget both in the SW and LW radiative energy spectrum (Shupe et al., 2004). The magnitude of the effect of clouds on the SEB will depend on the amount of cloud cover over the ice sheet and the optical thickness of the clouds (i.e. to what degree a cloud reflects or absorbs the incoming SW radiation passing through it, and its ability to absorb and emit LW radiation (van den Broeke et al., 2008b; AMS, 2012)). There is a competing influence on the SW and LW radiative energy spectrum from clouds over the GrIS which can either warm or cool the surface.

In the SW radiative energy spectrum, clouds can impact the amount of incoming SW radiation reaching the surface, which also alters the albedo of the surface (Shupe et al., 2004). The amount of SW radiation reaching the surface varies with changes in the cloud cover and cloud optical thickness. A reduction in cloud cover will increase the transmittance of the atmosphere allowing more incoming SW radiation at the-top-of-the-atmosphere to reach all the way down to the surface (Shupe et al., 2004). Conversely, an increase in cloud optical thickness will decrease the magnitude of SW radiation passing through the cloud (Shupe et al., 2004). As absorbed SW radiation over the ablation zone is the dominant energy source for surface melt over the GrIS, these are a crucial parameter for calculating the future (surface) mass balance. Recent studies indicate that a decrease in summer cloud cover driven by atmospheric circulation changes has largely driven the recent decrease in the SMB over the GrIS. Through satellite observations (running from 1995–2009) and climate model output, Hofer et al., 2017 found a significant reduction in summer (JJA) cloud cover over the southern and western parts of Greenland of 0.9 ±0.3% per year. With a reduction in summer clouds, more SW radiation was allowed over the (low albedo) ablation zone, increasing the yearly summer melt by 27 ±13 [Gt].

On the other hand, with an increase in cloud cover and cloud optical thickness follows an increase in emissivity of the clouds. This alters the LW radiative energy spectrum of the SEB by clouds 'trapping' heat emitted from the surface (Shupe et al., 2004). Through satellite observations, climate model data and snow model simulations, Van Tricht et al., 2016 found an enhanced meltwater runoff effect from a reduction in refreezing. With clouds reducing the radiative heat loss from the surface, they suggested that rather than a direct increase in meltwater production, there was a shift in the meltwater pathway from reduced refreezing, accelerating the bare-ice extent, thus enhancing the meltwater runoff. As opposed to this, Noël et al., 2019 found an increase in early-summer cloudiness over the north part of Greenland enhancing atmospheric warming through decreased LW heat loss from the surface (LWU in Equation (2.4)), and argued that this excess energy over the surface triggered a rapid snowline retreat over the ablation zone, causing early bare ice exposure and amplifying the runoff.

The total effect and efficiency from a change in clouds on the GrIS SEB will depend on internal factors, i.e. the exact microphysics of the cloud, as well as external factors such as the surface albedo (Fouquart et al., 1990).

2.3 Future projection of GrIS SMB change

The latest Intergovernmental Panel on Climate Change (IPCC) Assessment Report (AR)6 report states with high confidence that the total mass loss from the GrIS will continue to increase with cumulative emissions from human activity (Eyring et al., 2021). Coincidentally with rising temperatures and surface darkening over the GrIS, AR6 is also confident that increased meltwater runoff and reduced refreezing capacity over the ice sheet will be the predominant causes to future mass loss, rising to SMB reduction, in 21st century projections (Fox-Kemper et al., 2021).

Morlighem et al., 2017 estimated that the GrIS holds enough water for a total sea-level rise contribution of about 7.42 $\pm$ 0.05 m. Future sea-level rise is a threat to territorial integrity of small island states, coastal infrastructure and human habitat (Field, C.B. et al., 2014). Consequently, projections of future trajectories of the GrIS mass loss and subsequent sea-level rise contribution is important. The former AR5 and the Special Report on the Ocean and Cryosphere in a Changing Climate (SROCC) projected a sea-level rise contribution from the changes in the GrIS SMB of 0.07 (0.03 to 0.16) m in year 2100 under the high-emission scenario Representative Concentration Pathways (RCP)8.5 (Fox-Kemper et al., 2021). The latest AR6 stated a likely sea-level rise contribution of 0.13 (0.09 to 0.18) m under the high-emission scenario Shared Socio-economic Pathways (SSP)5-8.5 in year 2100 relative to 1995-2014. However, the absolute magnitude is still subject to uncertainties (Fox-Kemper et al., 2021). Since the former work of the AR5 and SROCC new emission scenarios and model development has been carried out.

Results from climate models participating in the Coupled Model Intercomparison Project (CMIP) of the World Climate Research Programme (WRCPR) sets the ground base for the IPCC reports. The CMIP was first organised in 1995 by the WRCPR Working Group on Coupled Modelling (WGCM), with the ambition to better understand past, present and future climate change. Their work include assessments of model performance, and quantification of what drives the spread in future climate projections. They specify experimental protocols and use the same climate scenarios, so climate outputs can be analysed collectively (WCRP, 2020). The CMIP outputs are further used to understand impacts of a changing climate, e.g. sea-level rise from glacial meltwater runoff (Chen et al., 2021). Their work has evolved in different phases, of which the sixth phase (CMIP6) is the latest.

The development on the CMIP6 climate and Earth system models include higher resolution, as well as incorporating better representation of the model physics, and chemical and biological processes (Chen et al., 2021). These upgrades in the CMIP6 models result in higher climate sensitivity, i.e. their warming response to a doubling of CO_2 concentration, compared to the previous CMIP5 effort (Meehl et al., 2020). The change in GrIS SMB is mostly controlled by atmospheric processes (Goelzer et al., 2020), thus one can directly link future near-surface warming to surface mass loss from the GrIS. Therefore, with higher warming in CMIP6 models due to greater climate sensitivity, one should expect stronger SMB loss from the GrIS when compared to the older CMIP5 models (Payne et al., 2021).

Hofer et al., 2020 found sea-level rise contribution from 2005–2100 of 7.9 cm more when using SSP5-8.5 in CMIP6 models compared to using the RCP8.5 in CMIP5 models. They attributed the differences mainly due to greater Arctic amplification signal with associated cloud and sea ice feedbacks in the SSP5-8.5 CMIP6 simulations. However, there is still uncertainty about whether this difference between CMIP5 and CMIP6 can only be attributed to the difference in warming between the models, or if there are other underlying mechanisms driving the difference in projected surface melt and runoff. Comparing the differences between CMIP5 and CMIP6 for a given temperature increase can give a better understanding of this, however this has not been done previous to this thesis.

CHAPTER 3

Methods

In this chapter we outline the research design in Section 3.1, introduce the regional model and the model setup used in Section 3.2, and the scenarios and selection of the GCMs used for downscaling in Section 3.3, before presenting the methods for computing anomalies in Section 3.4 and statistical significance in Section 3.5.

3.1 Research design

In the effort of achieving the objective of our study (Section 1.2), we want to investigate if SEB changes can partly explain the higher melt- and runoff- driven SMB loss with increasing temperature in CMIP6 models compared to CMIP5 models.

We base the analysis on three observations from the literature. First, CMIP6 models are associated with a more pronounced Arctic amplification signal compared to the previous CMIP5 models, despite using similar forcing levels for GHG emissions (Hofer et al., 2020). Therefore, to eliminate the confounding effect of greater general warming rates in CMIP6, we choose to look at the evolution of variables over the ice sheet for a given temperature increase, rather than at a fixed time at which each model will have warmed by a different amount. Second, significant amounts of extra energy are needed for melt-induced SMB loss from the GrIS (see Equations 2.2–2.4). Therefore, the analysis focuses on the long term changes in the SEB components as well as cloud components that may alter the SEB components, as possible physical drivers of SMB change. Third, as most melt occurs during the summer months June, July, August (JJA), a main focus is given on this season. However, as will be clear from the results in Chapter 4, the autumn months September, October, November (SON) are also of great importance to the difference in SMB evolution between CMIP5 and CMIP6, thus these will also be discussed throughout the study.

The data used for the analysis of this thesis is based on the same simulations as were used for segments of the work done by Hofer et al., 2020. They used a set of 11 high-resolution (15 km) regional climate model simulations over the GrIS. These simulations were conducted by using the regional climate model MAR to physically downscale six CMIP5 models and five CMIP6 models, using the RCP 8.5 and SSP 5-8.5 high-emission scenarios, respectively. For this study, we use the same 11 MAR simulations running from 1950 to 2100. However, further to previous studies we calculate different anomalies for various Greenland climate variables, i.e near-surface temperature, SMB, cloud cover and the SEB[1] based on the 1961-1990 mean state of each model simulation. Focusing on physical drivers of enhanced GrIS mass loss in CMIP6 at a given level of warming has not been studied in detail before and therefore will lead to novel insights into the future GrIS climate dynamics.

In turn, we use the anomalies for projecting any spatially averaged changes over the GrIS surface for a given temperature increase over 150 years (1950-2100), and compare these projections produced

[1] A full overview of all variables used for this analysis, with corresponding units, can be found in Table B.1 Appendix B.

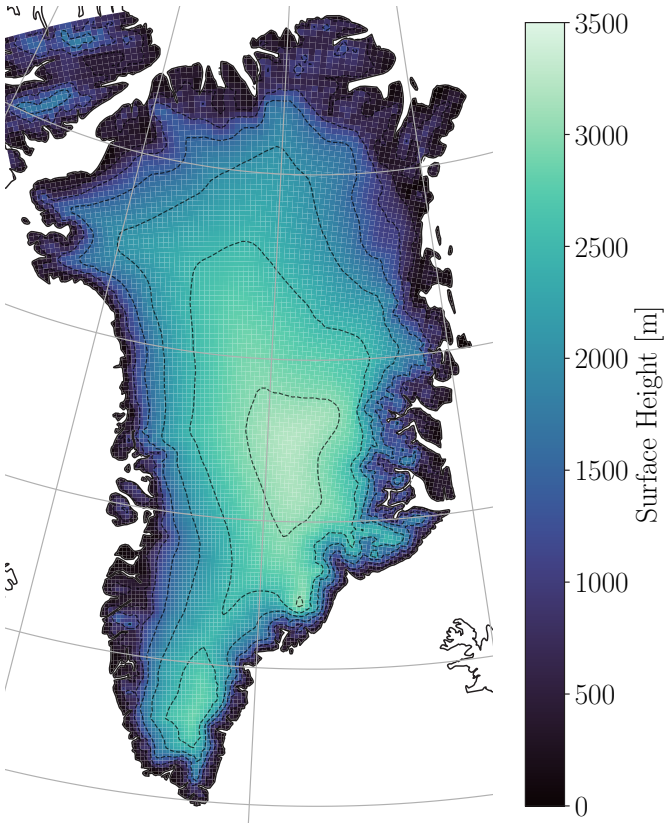

Figure 3.1: 15 km horizontal integration domain, and surface height over Greenland projected by the MAR simulations. Dashed lines indicate elevation curves running from 500 - 3500 masl. with 500 m interval.

by CMIP5 and CMIP6. Additionally, we look at a twenty-year averaged period of ∼4°C warming, to seek any potential differences in how changes in SMB, cloud cover, radiation and surface mass flux variables are spatially distributed over the ice sheet, to gain further insight into the spatial patterns of changes cause by rapid Greenland warming.

3.2 Regional Climate Modelling

RCMs are widely used in climate research and an important tool that enables us to produce climate information and gain process understanding over regional to local scales in more detail than what is allowed by GCMs (Rummukainen, 2010). Where GCMs have resolution on a scale of 100–200 km, strongly limiting their ability to realistically resolve local processes and dynamics, RCMs have much higher spatial resolution (typically 10–50 km) together with enhanced physics which can be optimised for distinct regions (Fettweis et al., 2013a; Doblas-Reyes et al., 2021).

Downscaling is a technique used for transforming coarse information from GCMs to more detailed information suitable for regional application. The two main approaches to downscaling are known as statistical and dynamical downscaling (Rummukainen, 2010). The former requires local weather observations to develop future climate data, by using the statistical relationship between historical outputs from the GCMs and the weather data. Dynamical downscaling can on the other hand be compared to a 'magnifying glass'. In this approach, RCMs take lateral boundary conditions as input from GCMs output, and rely on the same or more complex physics describing the dynamics of the climate processes of the GCMs (Dickinson et al., 1989; Rummukainen, 2010). However, as

the RCMs simulate at a higher spatial resolution, we are left with climate variable outputs from simulations that better resolve many relevant features, most notably topography, enabling us to analyse processes at a smaller scale (Rummukainen, 2010). For the purpose of this thesis we use a Polar Regional Climate Model that is able to capture the regional changes of the SMB over the GrIS.

Modéle Atmosphériqe Régional (MAR)

A widely used RCM over the polar regions is the Modéle Atmosphériqe Régional (MAR). The model consist of a three-dimensional atmospheric model[2], coupled to a one-dimensional energy-balanced based surface- and vegetation- model SISVAT[3] (Soil Ice Vegetation Atmosphere Transfer). In the atmospheric model, the full continuity equation is taken into account. It is a hydrostatic primitive equation model, where the vertical coordinates are normalised pressure-ratio coordinates, σ. These are obtained by normalising between the top- and surface-pressure of the model, described in Equation (3.1), by pressure (p), model-top pressure (p_t), and surface pressure (p_s).

$$\sigma = \frac{p - p_t}{p_s - p_t} \tag{3.1}$$

SISVAT models the exchange between the atmosphere and the surface. It is multilayered, and subdivided into a soil-vegetation module, and a snow-ice module, where the latter is based on the snow model CROCUS[4].

The radiative transfer through the atmosphere is largely influenced by clouds, so the cloud microphysical representation is of primary importance for controlling the SEB (Morrison et al., 2005). In MAR the cloud microphysical scheme is part of the hydrological cycle representation. MAR parameterizes the hydrological cycle through a single-momentum microphysical scheme[5], i.e. it uses one moment of the particle size distribution as the prognostic value. Moreover, cloud droplet and cloud ice concentration is taken into account in the calculation of the cloud optical depth (COD, i.e. cloud optical thickness) in MAR and is defined through the following equation as

$$\mathrm{COD} = \frac{3(W_w + W_i)}{2r_e} \tag{3.2}$$

with W_w and W_i representing the liquid water path and ice water path respectively, and $\mathrm{r}_e = xr_w + (1-x)r_i$ representing the effective cloud particle radius, where $\mathrm{x} = \mathrm{W}_w/(\mathrm{W}_w + \mathrm{W}_i)$, and r_w and r_i are the effective radii and droplet and ice crystal radius distribution respectively.

Further, the liquid water path is taken into account in the representation of cloud emissivity, e, through the following equation

$$e = 1 - \exp(-C_e(\mathrm{W}_w + \mathrm{W}_i)) \tag{3.3}$$

where $C_e = 0.13x + 0.05(1-x)$.

[2]For detailed description of the model see Gallée et al., 1994.

[3]For detailed description of model and coupling to the atmospheric model see De Ridder, 1998 and Fettweis et al., 2013a.

[4]For detailed description of the snow- and ice model CROCUS see Brun et al., 1992 and Vionnet et al., 2012.

[5]For detailed description of the parametrization of the hydrological cycle see Gallée, 1995.

MAR Greenland setup
For the work of this thesis, the MAR model physics and resolution remain unchanged across all simulations. The grid extent, projection and resolution of MAR[6] has been adapted specifically to the GrIS, whereas a slightly different model setup exists for Antarctica and other regions of the world. A summary of the MAR Greenland setup can be found in Table 3.1, and Figure 3.1 shows the integration domain produced through this setup.

Model version	3.9.6
Spatial resolution	15x15 km
Gridpoints	115x210 [lon,lat]
Integration domain, area	6.75x10^6 km^{-2}
Integration domain, coordinates	(-88,4°W,5.1°E) [lon] (54.89°N,85.92°N) [lat]
Integration time step	90 sec
Model-top pressure, p_t	0.1 hPa
No. pressure levels	24

Table 3.1: Summary of the MAR Greenland setup.

MAR requires input of lateral boundary conditions every six hours. This interval prevents the model from developing a fully-independent climate. At its lateral boundaries we provide six-hourly input on specific humidity, u- and v- wind components, temperature, and sea-level pressure, as well as daily input on sea-surface temperature and sea ice concentration.

It should be mentioned that SISVAT does not include a three-dimensional ice sheet model, therefore the ice extent and height over the GrIS is at a fixed level throughout the simulations. Additionally, as the focus of our analysis is on the response and changes over the ice sheet area of Greenland only, we mask out every pixel containing less than 10% ice cover.

3.3 MAR forcings

We use eleven MAR simulations (see Table 3.2) with monthly output data, running from 1st January 1950 until 1st of December 2100 for the analysis of this thesis. As mentioned in Section 3.1, we base our analysis on the same MAR simulations used for segments of the work done by Hofer et al., 2020. These were conducted through downscaling of projections from the same eleven GCMs.

Forcing fields	**Historical simulation**	**Future Scenario**	**CMIP phase**
ACCESS1.3	historical (1850–2005)	RCP8.5	5
CSIRO-Mk3-6-0	historical (1850–2005)	RCP8.5	5
HadGEM2-ES	historical (1850–2005)	RCP8.5	5
IPSL-CM5A-MR	historical (1850–2005)	RCP8.5	5
MIROC5	historical (1850–2005)	RCP8.5	5
NorESM1-M	historical (1850–2005)	RCP8.5	5
CESM2	historical (1850–2014)	SSP5-8.5	6
CNRM-CM6-1	historical (1850–2014)	SSP5-8.5	6
CNRM-ESM2-1	historical (1850–2014)	SSP5-8.5	6
MRI-ESM2-0	historical (1850–2014)	SSP5-8.5	6
UKESM1-0-LL	historical (1850–2014)	SSP5-8.5	6

Table 3.2: Forcing fields used to perform MAR simulations, historical periods and future scenarios of the simulations, and CMIP phase.

[6]For model evaluation of MARv3.9.6 see Delhasse et al., 2020.

Selection of the GCMs

Hofer et al., 2020 based their selection of CMIP models on the Ice Sheet Model Intercomparison Project (ISMIP) for CMIP6. In ISMIP they selected a 'top six' ensemble of CMIP5 models by first selecting a 'top three' ensemble following the ISMIP protocol (Barthel et al., 2020) (criteria 1-4) listed below. Thereafter, an additional three models were picked to maximise the projected diversity of the end of the century climate change projections, i.e. to capture the full diversity of the ensemble.

'Top three' models selection criteria:

1. The model must provide six-hourly outputs to provide as input to MAR at its lateral boundaries.
2. The model must provide six-hourly outputs for both the RCP2.6 and RCP8.5 scenario projections (with the latter being of importance for our study).
3. With regards to historical atmospheric, surface and subsurface ocean metrics, the model must lie in the upper half of the 33-model ensemble.
4. All climate change metrics of the model must lie within the two interquartile (i.e. not above 75% or below 25%) range of the multi-model median of the normalised projected change over the Antarctica and Greenland in 2100.

Due to delayed CMIP6 model data release, the model ensemble selection of CMIP6 models were not included in the ISMIP6. Therefore, Hofer et al., 2020's selection of the top CMIP6 models was limited by model availability at the time being. Only five out of seventeen available SSP5-8.5 CMIP6 models, met the first requirement of six-hourly outputs. However, in their study they found that the model ensemble of these five models in fact acceptably represented the model mean, minimum, and maximum of the full CMIP6 ensemble. Thus, all five models were included in the CMIP6 model ensemble for downscaling.

Scenarios

The eleven GCMs used as input for MAR were forced with historical simulations and high-emission future scenarios. Historical (1850-2005) emissions and the RCP8.5 (2006-2100) future emission scenario were used to force the six CMIP5 models. Updated historical emissions (1850-2014) and the SSP5-8.5 (2015-2100) future emission scenario were used to force the five CMIP6 models.

The RCP8.5 and SSP5-8.5 future scenarios are similar in the way that they approximately reach the same globally averaged forcing of +8.5 Wm^{-2} (i.e. the additional energy taken up by the Earth system as a consequence of an increased greenhouse effect) by the end of the 21^{st} century (O'Neill et al., 2016). However, they differ from each other in how they achieve this radiative forcing. The RCPs project trajectories of GHG concentrations and air pollutants from human activity and land use, they do not prescribe one specific socio-economic future, so that many possible futures leading to the same radiative forcing pathway may be used (Arias et al., 2021, p.21). Conversely, the SSPs are based on future narratives describing global development and projections of future emission and land use change from integrated assessment models (O'Neill et al., 2016; O'Neill et al., 2017).

3.4 Computation of anomalies

For the analysis of this thesis we calculate monthly, seasonal and annual anomalies from monthly MAR simulation outputs running from year 1950 to 2100. A thirty-year climatology is commonly used for atmospheric variables (van den Broeke et al., 2009), and so we base the calculation of our anomalies on a thirty-year averaged reference period running from 1961 to 1990, of which the GrIS was assumed to be in a stable state (van den Broeke et al., 2016). All anomalies have

been calculated individually for each of the MAR simulations forced by eleven GCMs, before being averaged over all six MAR simulations of CMIP5 models and over all five MAR simulations of CMIP6 models separately, hereby referred to as MAR CMIP5 and MAR CMIP6.

In particular, the annual anomalies are calculated as follows. First, a yearly mean of the monthly output is computed for every 15x15 km grid cell. Then, a reference period is produced by selecting and averaging over the thirty-year time period from 1961–1990. Further, the anomalies for every grid cell in each year are calculated by subtracting the reference from each year. This gives a time series of anomalies of 150 years, with a value for every variable in each grid point, every year. A spatial average is then calculated by taking the sum of a given variable in each grid point and dividing by the number of grid points.

The calculation of the monthly and seasonal anomalies are analogous to the calculation of annual anomalies, except that then we start off by using the monthly output directly or calculating the seasonal mean from the monthly outputs, respectively.

Twenty-year averaged warming period (+ 4°C $\pm$ 10 years)

For parts of our analysis we compare the MAR CMIP5 and MAR CMIP6 simulations for a period of similar warming. This we did by creating a moving average[7], with a centred window of 20 years, over the near-surface warming time series for each of the eleven MAR simulations individually. This allowed us to compute the arithmetic mean along the time series, where a 20 years ($\pm$ 10 years around each step) average for each year in the time series is returned. Then, by picking the year that returns a temperature closest to our designated near-surface temperature we can find the 20 years time interval for each model that should be of similar averaged warming.

Figure 3.2 (left) shows the moving averaged time series of the summer seasonal (JJA) near-surface temperature anomalies for each of our eleven MAR simulations, with a black horizontal line indicating a +4°C near-surface warming. We observe that there is a range of how fast the models warm, leading to a spread in what year each of them reach +4°C near-surface warming. The boxplots in figure 3.2 (right) gives an indication on the spread of temperature anomalies over the twenty-year warming period selected for each individual model. Here it generally looks like the models of strongest warming trends, e.g. UKESM, have a larger temperature range within the twenty-year warming period selected. The possible impacts of this will be further discussed in Chapter 5.

Now, from our 150 years time series of anomalies ranging from 1950–2100, we pick our twenty-year warming period for each model, before we average over all six MAR simulations of CMIP5 models and over all five MAR simulations of CMIP6 models separately.

This selection of a warming period can be done similarly for annual, monthly and other seasonal anomalies.

3.5 Statistical significance

We use two simple methods of testing statistical significance. First, in our projection of long-term change in climate variables as function of near-surface temperature increase, we fit a regression line to our mean model output. First, we want to be able to know if MAR CMIP5 and MAR CMIP6 projections are significantly different or not. Here, we calculate the standard deviation around the regression line, as a measure of variation around the line. If the interval of $\pm$ one standard deviation does not overlap between MAR CMIP5 and MAR CMIP6, we will consider the two projections significantly different. Second, we will use the coefficient of determination, R^2, to give an estimate

[7] We use a combination of the two Numpy functions *numpy.mean* and *numpy.roll*. Description of Numpys inbuilt function of numpy.mean and numpy.roll can be revised at
https://numpy.org/doc/stable/reference/generated/numpy.mean.html and
https://numpy.org/doc/stable/reference/generated/numpy.roll.html, respectively.

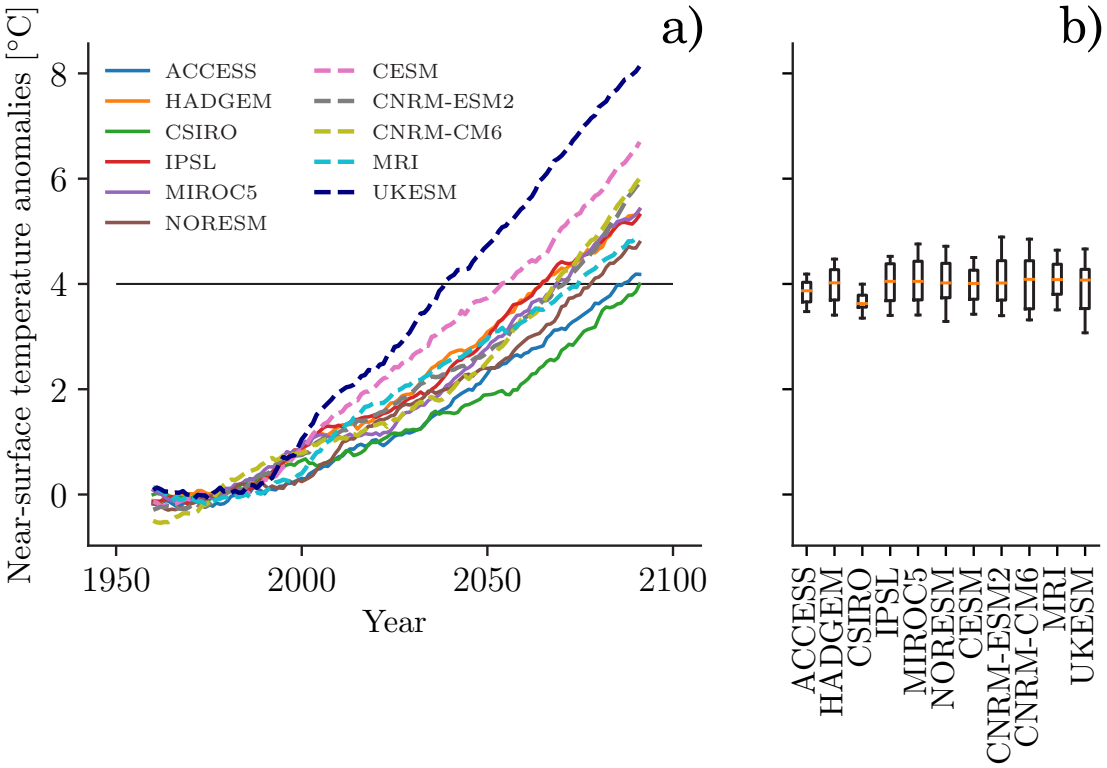

Figure 3.2: Moving average projection of near-surface temperature anomalies, and temperature variation within a twenty-year warming period of ∼4°C. a) A moving average of summer (JJA) near-surface temperature anomalies – spatially averaged over the Greenland ice sheet by taking the mean over all grid points – from individual model projections (1960–2090). The moving average is run over a time series of 150 years running from 1950 to 2100 with an averaging window of twenty years. Solid lines indicate CMIP5 models and dashed lines indicate CMIP6 models. **b)** boxplots showing the spread in summer temperature of the twenty-year +4°C warming period of each individual model selection. Orange line indicates the median temperature, box-bottom the first quartile (i.e. the lowest 25% values , box-top the third quartile (i.e the top 75% values), and top/bottom-whiskers the range of the temperature data.

on how well the fitted regression line represents the relationship of the observed variation for MAR CMIP5 and MAR CMIP6 separately.

Residual standard deviation

In our study we are looking at climate variables as a function of near-surface temperature. The residuals around a fitted regression line is the measured distance between the observed values, y_i, and the predicted values, $\hat{y}_i$. If the residuals around the regression line is small, then much of the variability in the observed values appears to be due to the relationship between the climate variable and the near-surface temperature. We can calculate the standard deviation around the fitted line through the following equation

$$\text{Residual Standard Deviation} = \sqrt{\frac{\sum(y_i - \hat{y}_i)^2}{(n-k)}} \tag{3.4}$$

where n is the number of observed data points and k is the degree of freedom associated with the estimate. To obtain the variance around the regression line, the parameters in the regression function must be estimated first, which results in a loss of k degrees of freedom depending on the regression function (Devore et al., 2018, p.631–633).

Coefficient of determination, R^2

We use the coefficient of determination, R^2, as a measure of how well the regression line represent the relationship of the observed variation. The total variation of our data points can be expressed as:

$$SST = \sum (y_i - \bar{y})^2 \tag{3.5}$$

i.e. the sum of all of the squares (SST) from our data points, y, to the mean of all data points, $\bar{y_i}$.

The variation of our data points around the fitted line can be expressed as:

$$SSE = \sum (y_i - \hat{y_i})^2 \tag{3.6}$$

i.e. the sum of squared error from the fitted line, where $\hat{y_i}$ is the predicted values by the line.

Then, the coefficient of determination, R^2, can be interpreted as the proportion of observed variation that can be explained by the fitted regression line:

$$R^2 = 1 - \frac{SSE}{SST} = 1 - \frac{\sum (y_i - \hat{y_i})^2}{\sum (y_i - \bar{y})^2} \tag{3.7}$$

The closer the R^2 is to 1, the greater is the proportion of observed variation that can be explained by the fitted regression line (Devore et al., 2018, p.632–634).

CHAPTER 4

Results

In this chapter we present the main results of this thesis. We focus on a comparison of anomalies for a given warming level between CMIP5 and CMIP6 to investigate whether the difference in the SEB and melt comes from a greater sensitivity at a given warming or just the fact that the GrIS warms more in CMIP6 than in CMIP5. In Section 4.1 we look at future projections of the GrIS SMB. In Section 4.2 we look at the radiative SEB and cloud properties that might affect the radiative SEB components. In Section 4.3 we look at the spatial distribution of essential GrIS climate components and in Section 4.4 we look at the temporal melt-albedo feedback and the SMB response.

4.1 GrIS Surface Mass Balance change

We will start by looking at the SMB over the GrIS. Figure 4.1 shows the annual, summer (JJA) and autumn (SON) seasonal SMB, melt and runoff anomalies [mmWE]. To obtain differences in GrIS SMB and melt between MAR CMIP5 and MAR CMIP6 coming from factors other than temperature, we compare the anomalies at a given near-surface temperature anomaly [°C]. Below we will try to disentangle the effect of greater warming in MAR CMIP6 from the differences resulting from strength variations in factors other than temperature.

First, in year 2100 we observe that across the MAR CMIP6 simulations there is a + 1.4°C greater warming over the GrIS than in MAR CMIP5 annually (+ 1.8°C in summer and autumn). This can be seen in Figure 4.1 because the MAR CMIP6 output extends beyond those from MAR CMIP5 on the x-axis. Consequently, MAR CMIP6 reaches a higher melt- (pink) and runoff anomaly (purple) and subsequently a greater surface mass loss (green), partly due to a higher near-surface temperature anomaly than what is found for MAR CMIP5.

Conversely, we also find a greater sensitivity of the GrIS SMB reduction in MAR CMIP6 even when looking at the same warming. In Figure 4.1 a) we see that MAR CMIP6 projects a higher annual melt and runoff anomaly for a given warming, and subsequently a greater surface mass loss, when compared to MAR CMIP5. Therefore, the data clearly suggests that parts of the greater mass loss in MAR CMIP6 over the GrIS are driven by a difference in SMB sensitivity for a given temperature change between the ensembles.

While we see a greater mass loss sensitivity annually, this difference is not necessarily spread equally across all seasons[1]. For example, during summer (JJA) we observe from Figure 4.1 b) that we have the largest absolute contribution of melt, runoff and SMB reduction for both MAR CMIP5 and MAR CMIP6 in a warming climate. However, the two ensembles project melt, runoff, and SMB similarly for a given temperature increase during summer. Conversely, from Figure 4.1 c) we find the largest difference in projected melt, runoff and SMB between MAR CMIP5 and MAR CMIP6 is coming from autumn (SON). Here, MAR CMIP6 projects a surface mass loss reduction of 14.1

[1]Here we only show the two seasons for summer and autumn. See Figure A.1 and Figure A.2 in Appendix A for winter (DJF) and spring (MAM) respectively.

± 4.8 mmWE for a temperature increase of + 6.7 °C, 12.5 mmWE more mass loss than for MAR CMIP5 at the same temperature increase (see Table 4.1). This suggests that the main driver of the greater mass loss sensitivity in MAR CMIP6 compared to MAR CMIP5 in the annual mean stems from the difference in sensitivity in autumn (SON).

Simulation	Variable	Unit	Near-surface temperature anomaly (±std) (JJA) 5.4°C	(SON) 6.7°C
MAR CMIP5	ALB	%	-6.0 (± 0.2)	-0.8 (± 0.1)
MAR CMIP6	ALB	%	-6.2 (± 0.3)	-1.4 (± 0.1)
MAR CMIP5	CC	%	2.4 (± 0.9)	2.9 (± 0.8)
MAR CMIP6	CC	%	-2.2 (± 1.1)	-0.7 (± 0.9)
MAR CMIP5	COD		0.30 (± 0.02)	0.08 (± 0.01)
MAR CMIP6	COD		0.30 (± 0.03)	0.10 (± 0.01)
MAR CMIP5	LHF	Wm^{-2}	5.0 (± 0.3)	1.2 (± 0.2)
MAR CMIP6	LHF	Wm^{-2}	4.9 (± 0.4)	1.7 (± 0.2)
MAR CMIP5	LW_{net}	Wm^{-2}	6.8 (± 0.8)	2.5 (± 0.4)
MAR CMIP6	LW_{net}	Wm^{-2}	4.4 (± 1.1)	1.5 (± 0.5)
MAR CMIP5	LWD	Wm^{-2}	29.2 (± 1.0)	27.9 (± 0.4)
MAR CMIP6	LWD	Wm^{-2}	26.8 (± 0.9)	27.1 (± 0.5)
MAR CMIP5	LWU	Wm^{-2}	-22.4 (± 0.2)	-25.4 (± 0.1)
MAR CMIP6	LWU	Wm^{-2}	-22.2 (± 0.2)	-25.4 (± 0.1)
MAR CMIP5	ME	mmWE	215.9 (± 4.8)	14.0 (± 1.4)
MAR CMIP6	ME	mmWE	222.5 (± 7.7)	22.9 (± 3.6)
MAR CMIP5	Net_{rad}	Wm^{-2}	16.4 (± 0.5)	2.7 (± 0.3)
MAR CMIP6	Net_{rad}	Wm^{-2}	16.5 (± 0.9)	2.1 (± 0.5)
MAR CMIP5	RU	mmWE	193.8 (± 6.5)	19.4 (± 1.9)
MAR CMIP6	RU	mmWE	198.6 (± 9.5)	31.1 (± 4.3)
MAR CMIP5	SMB	mmWE	-162.2 (± 7.0)	-1.6 (± 3.1)
MAR CMIP6	SMB	mmWE	-170.7 (± 9.2)	-14.1 (± 4.8)
MAR CMIP5	SHF	Wm^{-2}	2.1 (± 0.4)	-3.5 (± 0.4)
MAR CMIP6	SHF	Wm^{-2}	2.4 (± 0.5)	-2.6 (± 0.4)
MAR CMIP5	SW_{net}	Wm^{-2}	9.6 (± 0.9)	0.2 (± 0.1)
MAR CMIP6	SW_{net}	Wm^{-2}	12.1 (± 1.7)	0.6 (± 0.2)
MAR CMIP5	SWD	Wm^{-2}	-20.7 (± 2.0)	-2.5 (± 0.3)
MAR CMIP6	SWD	Wm^{-2}	-14.2 (± 1.8)	2.1 (± 0.5)

Table 4.1: MAR CMIP5 and MAR CMIP6 projected anomalies of climate variables for a given temperature increase, associated units, and ± one standard deviation given in brackets. The standard deviation is calculated for a 20 year interval prior the selected warming. Temperature increase of + 5.4°C + 6.7°C is selected for summer (JJA) and autumn (SON) respectively, representing the close to end temperature for the MAR CMIP5 projections where it deviates the most from MAR CMIP6.

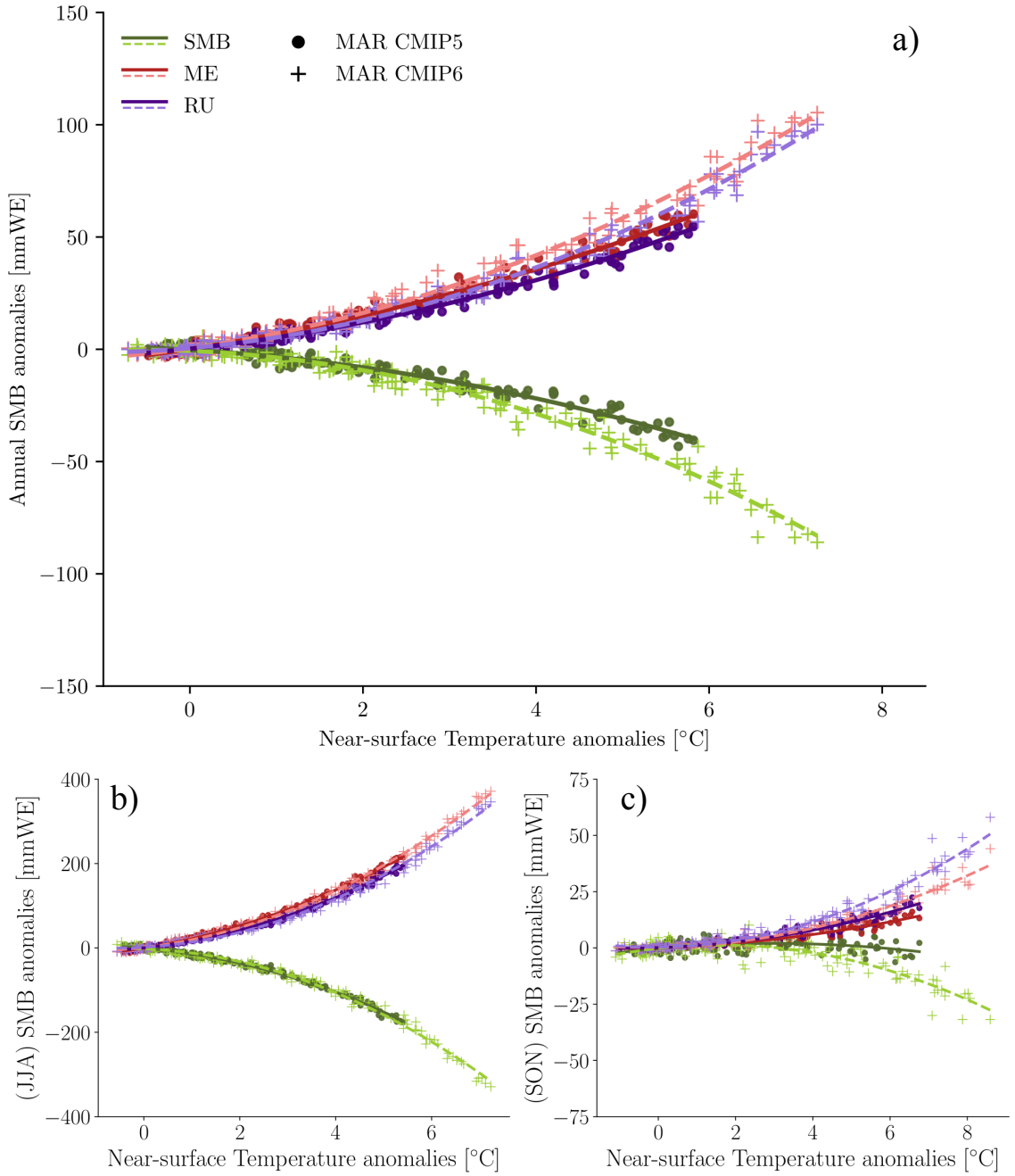

Figure 4.1: SMB, melt and runoff anomalies [mmWE] over the GrIS as a function of near-surface temperature anomalies [°C]. a) Annual SMB-, melt- (ME), and runoff anomalies (RU) [mmWE] over the GrIS as a function of annual near-surface temperature anomalies [°C] from MAR CMIP5 (dots) and MAR CMIP6 (crosses), with regression drawn in solid lines for MAR CMIP5 and scattered lines for MAR CMIP6. All anomalies are related to the thirty-years averaged reference period (1961–1990). **b)** and **c)** same as **a)**, but for a seasonal mean of summer (JJA) and autumn (SON), respectively. Regression equation and R^2 score can be found in Table B.2 in Appendix B.

4.2 Cloud contribution to Surface Energy Budget change

In the process of understanding where the projected difference in surface mass loss between MAR CMIP5 and MAR CMIP6 comes from, we look at the energy at the surface of the ice sheet available for melt or warming of the snowpack. Here, we focus on the radiative energy flux components from the SEB (see Equation (2.4)), because the radiative energy fluxes haven been shown to be the main contributor to melt and surface mass loss over GrIS (van den Broeke et al., 2009; Fettweis et al., 2013a). Figure 4.2 shows the seasonal radiative surface energy flux components anomalies ([Wm^{-2}], top) and the seasonal cloud cover anomalies ([%], bottom) as a function of the seasonal near-surface temperature anomalies [°C] for the summer season (JJA, left) and autumn season (SON, right).

First, as for the SMB components in Figure 4.1 we also observe in Figure 4.2 that across both ensembles and for both seasons MAR CMIP6 reaches a greater warming of + 1.8°C in 2100 compared to MAR CMIP5. However, as we aim to distinguish the contribution from more absolute warming to that from greater sensitivity, our focus remains on the differences between MAR CMIP5 and MAR CMIP6 for a given warming.

In Figure 4.2 a), showing the summer (JJA) seasonal radiative SEB components anomalies [Wm^{-2}] as a function of summer near-surface temperature anomaly [°C], we observe that the net radiative flux (grey) is behaving similarly for MAR CMIP5 and MAR CMIP6 for a given near-surface temperature increase. However, shortwave and longwave components composing the net radiative flux show different behaviour between MAR CMIP5 and MAR CMIP6. Firstly, we can observe that there is more net shortwave radiation (SW_{net}, yellow) reaching the surface in MAR CMIP6 compared to MAR CMIP5 for a given temperature increase. This difference seems to mainly come from more shortwave downward radiation (SWD, purple) reaching the surface in MAR CMIP6. Secondly, we see that there is less net longwave flux (LW_{net}, blue) absorbed at the surface in MAR CMIP6 compared to MAR CMIP5. The amount of outgoing longwave radiation emitted from the surface (LWU, green) is behaving similarly between MAR CMIP5 and MAR CMIP6, so the difference we observe in LW_{net} seems to be coming from a decrease in downwelling longwave radiation (LWD, red) for a given temperature increase in MAR CMIP6.

Conversely, in Figure 4.2 b), showing the autumn seasonal (SON) SEB components anomalies as a function of autumn near-temperature anomalies, we observe a similar behaviour between MAR CMIP5 and MAR CMIP6 for the entire ensemble of radiative fluxes (i.e. LWD, LWU, LW_{net}, SWD, SW_{net}, and Net radiative flux).

Overall, for both summer and autumn we observe a similar general behaviour with warming temperatures from MAR CMIP5 and MAR CMIP6 of increasing SW_{net} that seem to be coming from the melt-albedo feedback and darker surfaces despite decreasing SWD, concurrently as LWD is increasing with warming. However, for a given temperature increase we observe more SWD and less LWD reaching the surface in MAR CMIP6 in summer (Figure 4.2 a)). Recalling (Equation (2.4)) on the SEB, the difference in summer LWD and SWD between MAR CMIP5 and MAR CMIP6 can possibly be linked to differences in cloud properties. A change in cloud cover and the transmissivity of the atmosphere can affect the amount of SWD reaching the surface, as well as the atmospheric longwave emissivity, which is directly linked to the LWD. Therefore, it is essential to investigate the cloud properties over the ice sheet and their differences between MAR CMIP5 and MAR CMIP6.

Figure 4.2 c), showing the seasonal (JJA) cloud cover anomalies as a function of summer near-surface temperature anomalies, displays an increasing cloud cover in MAR CMIP5 of + 2.4 ± 0.9 %, whereas MAR CMIP6 shows a decreasing cloud cover of - 2.2± 1.1 % for a near-surface warming of + 5.4°C (see Table 4.1). While the magnitudes of the changes in cloud cover are the same between MAR CMIP5 and CMIP6, we see a completely different behaviour in terms of the sign of the change. In MAR CMIP5 cloud cover in summer increases with warming, while in MAR CMIP6 cloud cover over the GrIS notably decreases for a given warming.

Similarly, for autumn (SON) we observe an increase in cloud cover in MAR CMIP5 of + 2.9 ± 0.8 % and a decrease in MAR CMIP6 of - 0.7 ± 0.9 % for a + 6.7°C near-surface warming (Figure 4.2

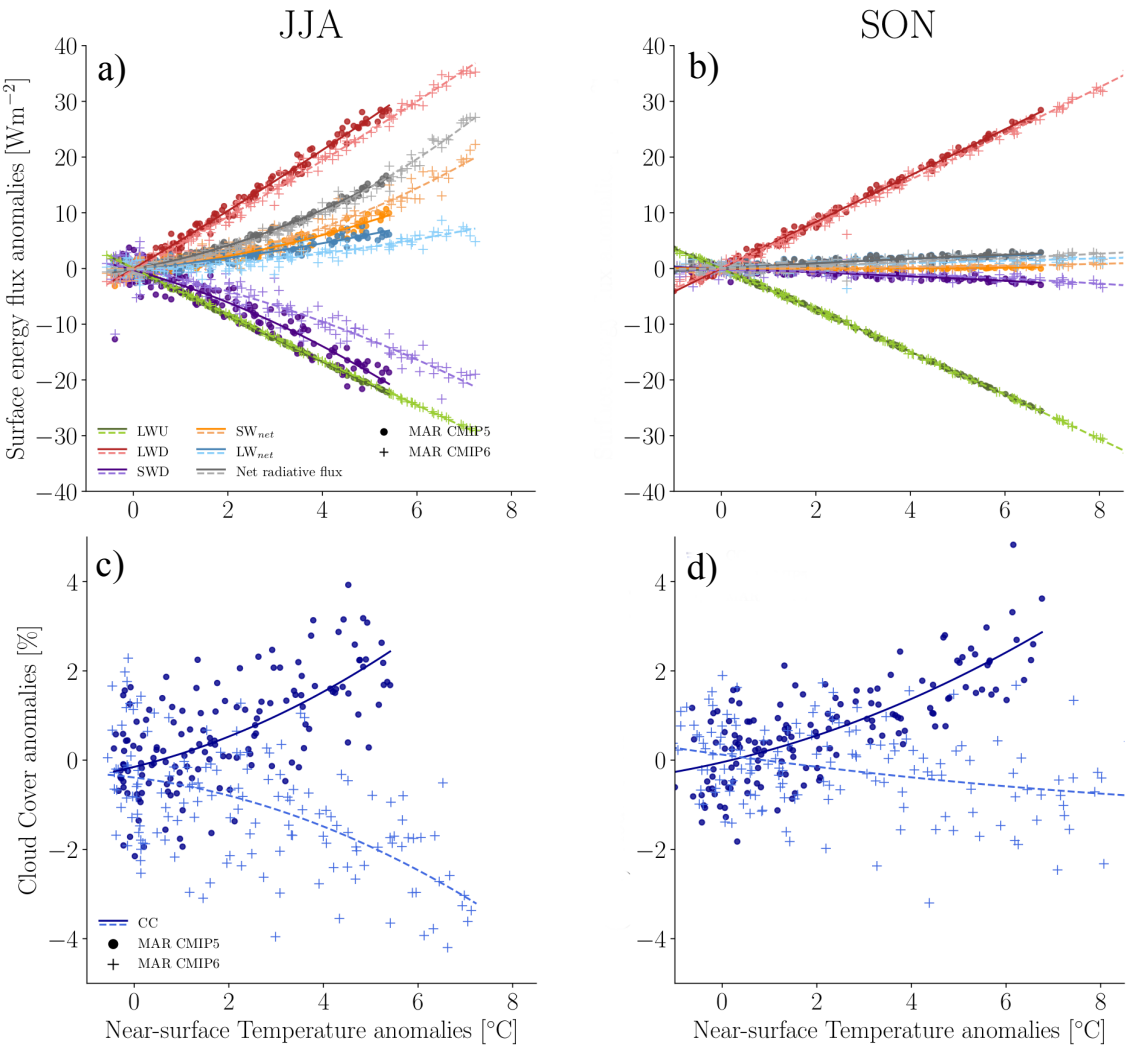

Figure 4.2: Radiative SEB component anomalies [Wm^{-2}] and total cloud cover anomalies [%] as a function of the near-surface air temperature anomalies [°C]. a) Seasonal (JJA) radiative SEB component anomalies [Wm^{-2}] over the GrIS according to near-surface air temperature anomalies [°C] from MAR CMIP5 (dots) and MAR CMIP6 (crosses), with regression drawn in solid lines for MAR CMIP5 and dashed lines for MAR CMIP6. It includes the radiative energy fluxes of longwave down (LWD), longwave up (LWU), shortwave down (SWD), net longwave radiation (LW$_{net}$), net shortwave radiation (SW$_{net}$), and Net radiative flux. Positive direction towards the surface. **b)** same as **a)**, but for autumn (SON). **c)** same as **a)**, but for the variable of cloud cover [%]. **d)** same as **c)**, but for autumn (SON). Regression equation and R^2 score can be found in Table B.2 in Appendix B.

d) and Table 4.1). Thus, the magnitude of the difference in cloud cover changes between MAR CMIP5 and MAR CMIP6 is largest in summer, however MAR CMIP5 and MAR CMIP6 show a diverging behaviour in terms of cloud cover anomalies over both seasons.

The decrease in cloud cover observed in MAR CMIP6 likely explains why we also see more SWD reaching the surface in summer in MAR CMIP6 compared to MAR CMIP5 (Figure 4.2 a)) as the

transmissivity of the atmosphere changes with the magnitude of cloud cover (see Section 2.1). This will disproportionately affect the darker bare ice areas of the ablation zone, where a large fraction of this extra shortwave energy is absorbed.

Figure 4.3 a), showing the Cloud Optical Depth (COD) anomalies as a function of near-surface temperature anomalies for summer (JJA), we observe a similar behaviour between MAR CMIP5 and MAR CMIP6 of increasing COD with warming. Recalling Equations 3.2–3.3, this change in cloud phase of increasing COD will increase the emissivity, which is in line with the general pattern of increasing LWD we observe from both simulations. Moreover, with increasing COD the transmissivity of the atmosphere decreases, allowing less solar radiation reaching the surface which we observe by the general pattern of decreasing SWD in both simulations. However, there is no significant difference in COD anomalies between MAR CMIP6 and CMIP5 in summer (JJA), hence COD seems not to explain the differences in LW and SW radiative flux between the two simulations in summer (JJA). Therefore, we suggest the high amount of SWD reaching the surface of the GrIS in MAR CMIP6 is only a direct consequence of the decrease in cloud cover with warming during summer (JJA). Because we do not see major differences in cloud optical depth, we can likely rule out a notable contribution from changes in cloud microphysics between MAR CMIP5 and MAR CMIP6 over Greenland (i.e. water phase changes) in summer.

Conversely, in autumn (SON, Figure 4.3 b)) there is a small difference in COD anomaly. We see an increase of + 0.08 ± 0.01 in MAR CMIP5 and + 0.1 ± 0.01 in MAR CMIP6 for a + 6.7°C near-surface temperature warming (Table 4.1). For autumn (SON), the data therefore suggest that more optically thick clouds counteract the effect of cloud cover reduction in MAR CMIP6, thus we observe no difference in the SW and LW radiative energy fluxes between MAR CMIP5 and MAR CMIP6 at a given warming.

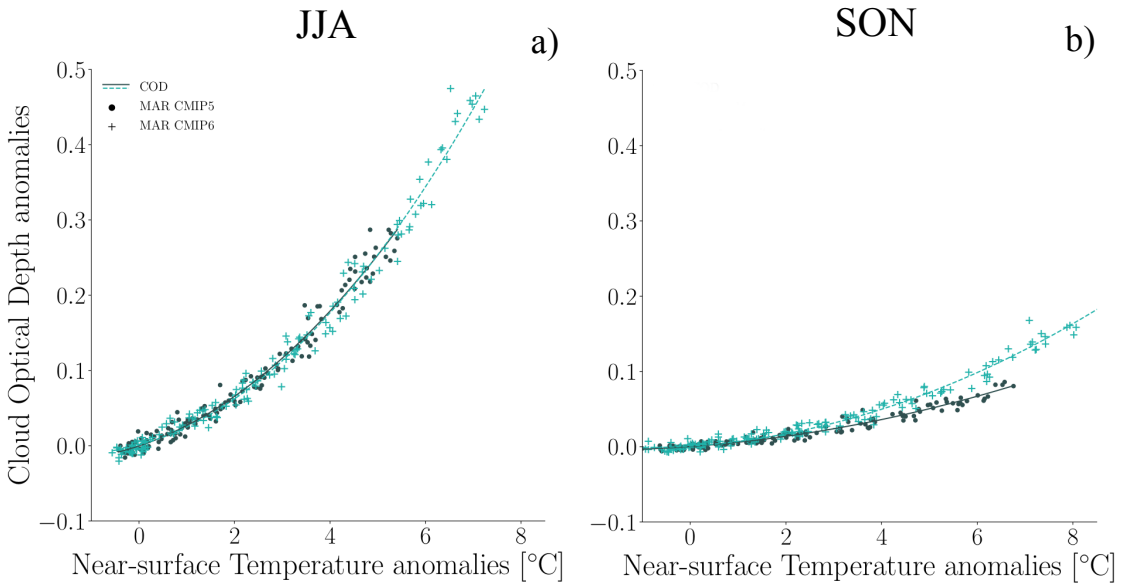

Figure 4.3: Cloud Optical Depth anomalies over the GrIS according to near-surface temperature anomalies [°C].a) Summer (JJA) Cloud Optical Depth (COD) anomalies over the GrIS as a function of annual near-surface temperature anomalies [°C] from MAR CMIP5 (dots) and MAR CMIP6 (crosses), with regression drawn in solid lines for MAR CMIP5 and scattered lines for MAR CMIP6. All anomalies are related to the thirty-year average reference period (1961–1990). **b)** same as **a)** but for autumn (SON). Regression equation and R^2 score can be found in Table B.2 in Appendix B.

4.3 Spatial distribution over the GrIS

In this section we will explore how the cloud- and radiative SEB- components, SMB, melt, runoff and refreezing are spatially distributed over the GrIS for a twenty-year warming period (+ 4 °C ± 10 years) compared to the thirty-year averaged reference period (1961–1990).

Overall, we see a spatially homogeneous pattern when we compare the different cloud cover responses over the GrIS in summer (Figure 4.4, left). While we observe an overall increase in cloud cover in MAR CMIP5 with warming over most of the GrIS in summer (Figure 4.4 left, top), we see a decrease in MAR CMIP6. Due to the homogeneous nature of the difference between MAR CMIP6 and MAR CMIP5 (Figure 4.4 "(CMIP6-CMIP5)") we argue that differences in circulation are unlikely to be the driver behind this difference in cloud cover response with warming, as circulation-driven cloud cover changes would be expected to result in a more distinct spatial pattern in areas with anomalous upslope and downslope winds. Additionally, the data also suggests that this pattern in cloud cover stems mostly from a contrasting behaviour in upper-level clouds (Figure 4.4 left, bottom), while mid- and low-level clouds do not seem to behave very differently (see Figure A.4 in Appendix A). We expect this homogeneous pattern of cloud cover reduction in MAR CMIP6 to lead to a greater proportion of shortwave radiation reaching large parts of the surface of the GrIS in summer in MAR CMIP6.

Looking at the cloud cover response over the GrIS in autumn (Figure 4.4, right), we detect similar patterns of cloud cover between MAR CMIP5 and MAR CMIP6, but of different magnitude. In the total cloud cover (Figure 4.4 right, top), MAR CMIP5 shows increasing cloud cover over most regions of the ice sheet, with an exception of a modest decrease over the extreme south-east. In the north-west area where MAR CMIP5 shows its strongest positive cloud cover anomaly, MAR CMIP6 only shows a modest increase, whereas the rest of the ice sheet in MAR CMIP6 experiences a decrease in cloud cover. We also see a more negative cloud cover anomaly over the whole ice sheet in MAR CMIP6 when compared to MAR CMIP5 ("(CMIP6-CMIP5)" Figure 4.4 right, top). Again, the data also suggests for the autumn clouds that this pattern in cloud cover stems mostly from a contrasting behaviour in upper-level clouds (Figure 4.4 right, top), while mid- and low-level clouds do not seem to behave very differently (see Figure A.5 in Appendix A).

Overall, when comparing the cloud cover over the GrIS from MAR CMIP5 and MAR CMIP6, we see that MAR CMIP6 produces more negative cloud cover anomalies in both seasons, with the strongest difference seen in the summer cloud cover. We will not go any further into investigating where this difference in cloud behaviour stems from in this chapter, however a discussion on possible origins will be addressed in Chapter 5. Instead, we continue by looking into how this change in cloud pattern affects the radiative energy fluxes over the GrIS.

Figure 4.5 shows the difference in anomaly of the radiative SEB components between MAR CMIP6 and MAR CMIP5 for summer (JJA, left) and autumn (SON, right). First, we take a look at the left panel showing the difference in summer (JJA) anomalies. The two uppermost maps show a more negative downwelling of LW radiative flux (LWD) anomaly, and a more positive downwelling of SW radiative flux (SWD) anomaly reaching the surface in MAR CMIP6 compared to MAR CMIP5 over most of the ice sheet. This corresponds with what we expected from the homogeneous cloud cover reduction in summer in MAR CMIP6, increasing the transmissivity of the atmosphere. Then, if we look at the second to last map, we also see an overall more negative anomaly of net LW radiation over the GrIS for MAR CMIP6. With a smaller amount of LWD radiative flux over the GrIS from the reduction of cloud cover, we expect there to be less heat trapped, hence less warming of the snowpack from LW radiation. Finally, looking at the bottom plot, we see that partly because there was an overall more positive SWD radiation over the ice sheet, we have more positive net SW radiation anomalies in MAR CMIP6 concentrated along the edges where we find the dark ablation zone. We also see an interesting band of slightly negative net SW radiation just above the ablation zone. We suspect this pattern to stem from the influence of reduced cloud cover over an area where clouds usually warm the highly-reflective surface, i.e. less clouds cool the surface. Therefore, due to a reduction in clouds in CMIP6 the net energy flux is reduced above the ablation zone, leading

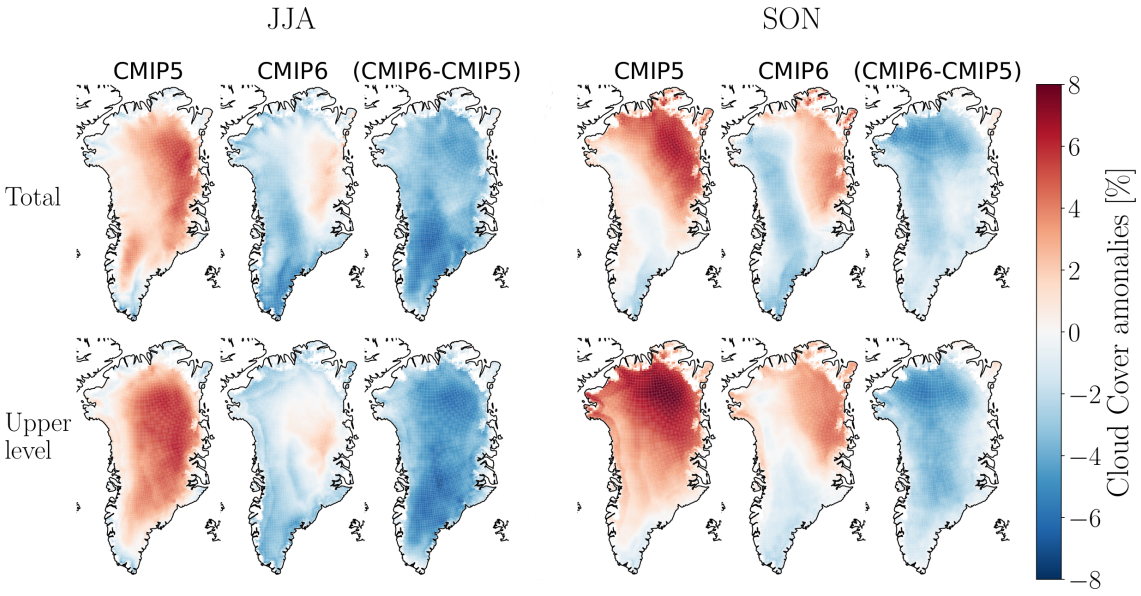

Figure 4.4: Cloud cover anomalies [%] for MAR CMIP5 and MAR CMIP6 simulations (+ 4 °C ± 10 years) for summer (JJA) and autumn (SON). Twenty-year average (4 °C ± 10 years) of the cloud cover [%] over the GrIS) for summer (JJA, left) and autumn (SON, right). The two rows indicate the total (upper row) and upper level cloud cover (bottom row). Each season has three columns — the first indicates the cloud cover anomalies for MAR CMIP5, the second for MAR CMIP6, and the third the difference between the two (CMIP6-CMIP5). For MAR CMIP5 and MAR CMIP6 a positive value (red) indicates an increase in cloud cover, and a negative value (blue) a reduction in cloud cover compared to the reference period. For the difference (CMIP6-CMIP5) a positive value (red) indicates more positive cloud cover anomaly, and negative values (blue) indicate a more negative cloud cover anomaly in MAR CMIP6 compared to MAR CMIP5.

to less melt over the bright surface and therefore a less pronounced melt-albedo feedback, causing a reduction in absorbed shortwave radiation in MAR CMIP6. Over all of the accumulation zone the snowpack will usually reflect more of the incoming SW radiation and a reduction in cloud cover therefore leads to a cooling of the snowpack. Conversely, in the darker ablation zone where more bare ice is exposed, more of this extra SWD radiation in MAR CMIP6 can be absorbed and lead to more melt or warming of the surface. This will be further addressed in Section 4.4.

We also observe an overall more negative cloud cover anomaly in MAR CMIP6 in autumn (SON), however with a reduced strength compared to summer (JJA). Looking at the difference in anomalies for the radiative SEB for autumn (SON) we expect similar changes as we saw for summer, but with reduced magnitude. In autumn (SON, Figure 4.5 right panel), we see a more negative anomaly of LWD over most of GrIS, with an exception along the east coast where there seems to be a modest positive anomaly in MAR CMIP6 compared to MAR CMIP5. As for summer (JJA), we also observe an overall more negative anomaly for net LW radiation across the whole ice sheet, however of smaller magnitude. Modest positive anomalies are also detected for SWD across most of the ice sheet, however slightly less on the extreme south-east. Therefore, we suspect the more positive net SW radiation anomalies – mostly centred around the southern ablation zone – to come from a darker surface created in summer and still being exposed over the lower ablation zone during autumn. We expect this change in SW radiation around the lower ablation zone to enhance autumn melt and runoff over the lower ablation zone. Thus, we continue with further investigation of the SMB over the GrIS.

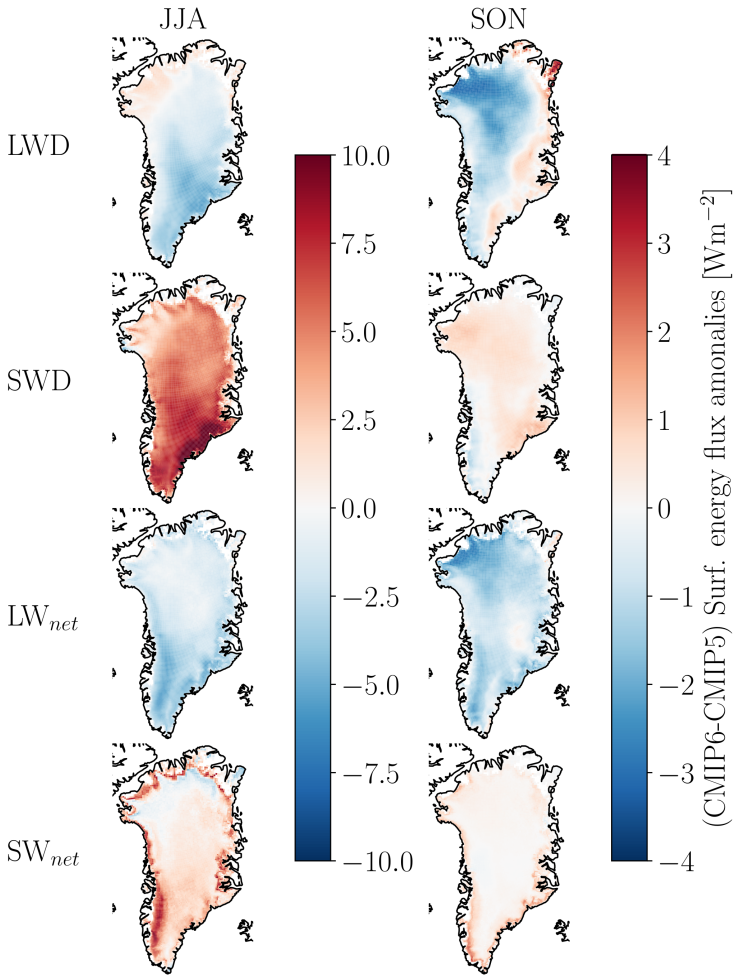

Figure 4.5: Difference in anomaly of SEB fluxes between MAR CMIP6 and MAR CMIP5 simulations (+ 4°C ± 10 years) for summer (JJA) and autumn (SON). Twenty-year average (+ 4°C ± 10 years) difference in SEB. The two columns indicate the mean difference of the anomalies for summer (JJA) (left) and autumn (SON) (right). Positive value (red colours) indicate a greater amount of energy flux reaching the surface in MAR CMIP5 compared to MAR CMIP6, whereas negative values (blue colors) indicates less amount of energy flux reaching the surface in MAR CMIP6 compares to MAR CMIP5.

Figure 4.6 shows the difference in anomaly of SMB, melt, runoff and refreezing between MAR CMIP6 and MAR CMIP5 for summer (JJA, left) and autumn (SON, right). First, we take a look at the left panel showing the difference in summer (JJA) anomalies. The uppermost map shows a greater negative SMB anomaly over most of the ablation zone, and a greater positive SMB in the transition zone between the ablation and accumulation zones (i.e. the percolation zone) in MAR CMIP6 compared to MAR CMIP5. Recalling from Equations 2.1–2.3, to have a reduction in surface mass, meltwater must leave the ice sheet through runoff. From top down the second and third map show more positive melt and runoff anomalies along the same area of the ablation zone experiencing more negative SMB anomalies. Thus, the more negative SMB anomalies in MAR CMIP6 seem to be coming from a more positive melt and runoff anomaly in the same area, most likely induced by more absorbed SW radiation. Conversely, in the percolation zone where more positive SMB anomaly was detected, we suspect an effect of more positive refreezing anomaly (lowermost map) and subsequent more negative runoff (last to lowermost map) in MAR CMIP6.

Most likely, despite enhanced SW radiation due to less clouds, the disproportionate decreased incoming LW radiation reduces the bare ice exposure in the percolation zone where the residual snowpack is usually thicker and reflects sunlight more efficiently for longer. Thus, the ice sheet experiences less melt and runoff, and more refreezing in this area during summer (JJA). The effect of more negative SMB anomalies in the ablation zone seems to cancel out the effect of more positive SMB anomalies over the percolation zone, thus no difference is detected between MAR CMIP6 and MAR CMIP5 in the spatially averaged SMB projections with warming in Figure 4.1 b) in summer (JJA).

In autumn (SON) we do not see the same buffering effect of more refreezing in MAR CMIP6 in the percolation zone as we saw for summer (JJA). The uppermost map in the right panel of Figure 4.6 shows more negative SMB anomalies mostly over the ablation zone, concentrated around the southern tip of the ice sheet, between MAR CMIP6 and MAR CMIP5. Over the lower parts of the ablation area in the south of the ice sheet we also see more positive melt (second map) and runoff anomalies (third map) in MAR CMIP6 than MAR CMIP5. We suspect that the excess SWD reaching the surface in MAR CMIP6 in summer (JJA) induces a stronger surface darkening of the lower ablation zone, thus enhancing the surface mass loss in autumn (SON) where the bare ice is still exposed. With a reduced buffering effect of refreezing in the percolation zone (fourth map), compared to summer (JJA), we detect a total difference in the spatially averaged autumn SMB projections with warming between CMIP6 and CMIP5 from more melt and runoff in the darker ablation zone. This can be further investigated by looking at the albedo effect.

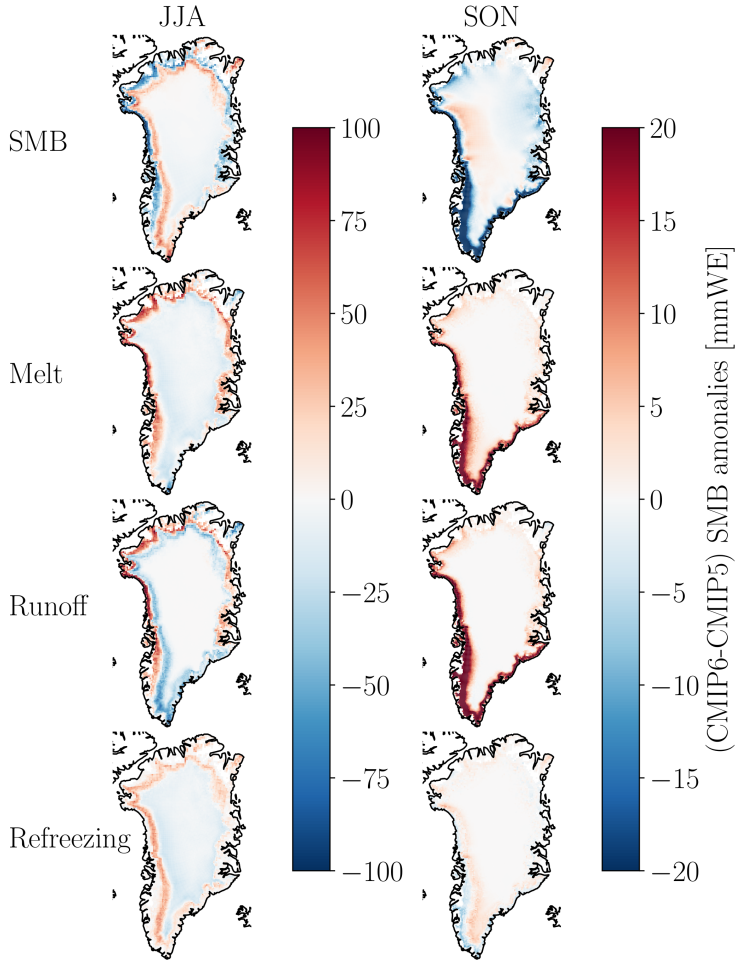

Figure 4.6: Difference in anomaly of selected SMB components between MAR CMIP6 and MAR CMIP5 simulations (+ 4°C ± 10 years) for summer (JJA) and autumn (SON). Twenty-year average (+ 4°C ± 10 years) difference in anomalies of melt, runoff, refreezing and the total SMB [mmWE], of MAR (CMIP6-CMIP5). Anomalies are related to the reference period (1961–1990). The two columns indicate the mean difference of the anomalies for summer season (JJA, left), and autumn season (SON, right). Positive values (red) indicate a greater mass balance at the surface in MAR CMIP6 compared to MAR CMIP5, while negative values (blue) indicate a lower mass balance in MAR CMIP6 compared to MAR CMIP5.

4.4 Melt-albedo feedback response

The magnitude of the surface albedo will determine how much incoming SW radiation will be reflected or absorbed by the surface. Future changes in the strength of the melt-albedo feedback will therefore play a leading part in how much energy is available for melt over the GrIS surface. Figure 4.7 shows the seasonal albedo anomalies [%] as a function of the seasonal near-surface temperature [°C](top) and how the differences "(CMIP6-CMIP5)" in albedo anomalies are spatially distributed over the ice sheet for a twenty-year averaged warming period (+ 4°C ± 10 years), for summer season (JJA, left) and autumn season (SON, right).

First, starting with summer. We detect a decrease in the spatially averaged albedo anomaly for a given seasonal near-surface temperature anomaly for both MAR CMIP5 and MAR CMIP6 in summer (JJA, Figure 4.7 a), the well-known melt-albedo feedback. We can also clearly see from

this plot that there is no difference in the spatially averaged albedo anomalies between MAR CMIP5 and MAR CMIP6. However, looking at the differences in spatial summer (JJA) distribution between MAR CMIP5 and MAR CMIP6 (Figure 4.7 c), we observe more negative anomalies in the ablation zone around the ice sheet, with the exception of the south-east coast. We think this darkening of the surface owes to more SW radiative flux over the ablation zone of bare ice, induced from decreasing cloud cover in MAR CMIP6. This surplus of SWD radiation in CMIP6 leads to more melt over the dark ablation zone, enhancing surface darkening.

Conversely, we observe more positive anomalies over parts of the percolation zone in MAR CMIP6. We suspect that parts of the percolation zone in MAR CMIP6 experience a surface cooling, as a result of less LW radiation reaching the surface, stemming from the reduction in cloud cover. Therefore, we think that this layer has a higher albedo because there is winter snow in this area that has experienced less long-lasting melt events in MAR CMIP6. We then suggest that the more negative albedo anomaly detected in the ablation zone and the more positive albedo anomaly in the percolating zone cancel each other out, and therefore we can not detect any difference in the spatially averaged projection of the albedo between MAR CMIP6 and MAR CMIP5 in summer (JJA).

In autumn (SON, Figure 4.7 b) we also observe a decrease in albedo anomalies with increasing near-surface temperature anomalies for both MAR CMIP5 and MAR CMIP6. From Table 4.1 we see that for a given temperature warming of 6.7° MAR CMIP5 projects a decrease in albedo of -0.8 $\pm$ 0.1 and -1.4 $\pm$ 0.1 in MAR CMIP6. When looking at the spatial distribution of the difference in albedo anomalies between MAR CMIP6 and MAR CMIP5 (Figure 4.7, d) we see a widespread negative albedo anomaly around the outer ablation zone. This lower albedo in autumn in MAR CMIP6 we think, is due to the fact that the higher ablation zones get covered with snow during autumn (SON) first. However, the lower ablation zone experienced more melt and runoff in summer due to less clouds, and therefore is darker coming into autumn. Here, the bare ice is still exposed in the lower ablation zone, leading to more absorption of SW radiation and surface melt in the autumn (SON), without a buffering effect from extra refreezing that we observed in summer (JJA).

Figure 4.8 shows the annual cycle of albedo (top) and SMB (bottom) in absolute numbers from monthly outputs of MAR CMIP5 and MAR CMIP6 for both the thirty-years averaged reference period (1961–1990) and the twenty-year averaged warming period (+ 4 $\pm$ 10 years). From the annual cycle of albedo we can observe that for both MAR CMIP5 and MAR CMIP6 the cycle of the warming period starts to deviate from their reference period in May, before reaching their strongest reduction in albedo in July. However, in July MAR CMIP6 reaches a lower albedo than MAR CMIP5, and stays at a lower magnitude until they reach the same level of albedo between October and November. In other words, the ice sheet is getting darker and stays darker for longer in MAR CMIP6 compared to MAR CMIP5.

Looking at the annual cycle of SMB we can detect some of the same patterns. First, we note that both MAR CMIP5 and MAR CMIP6 warming cycle starts to deviate from their reference in may, thus reach a state where the ice sheet is loosing more surface mass than what it is gaining (i.e. SMB<0) between May and June. Then, in July both MAR CMIP5 and MAR CMIP6 reach their lowest values of SMB. From here on, we observe that MAR CMIP5 is reaching a state where it is gaining mass faster than MAR CMIP6, and that MAR CMIP6 more slowly reaches the same winter state of SMB. Overall, we then see an effect over the ice sheet where the MAR CMIP6 models show a longer period of SMB < 0 which corresponds to the same period where the albedo is lower than for MAR CMIP5.

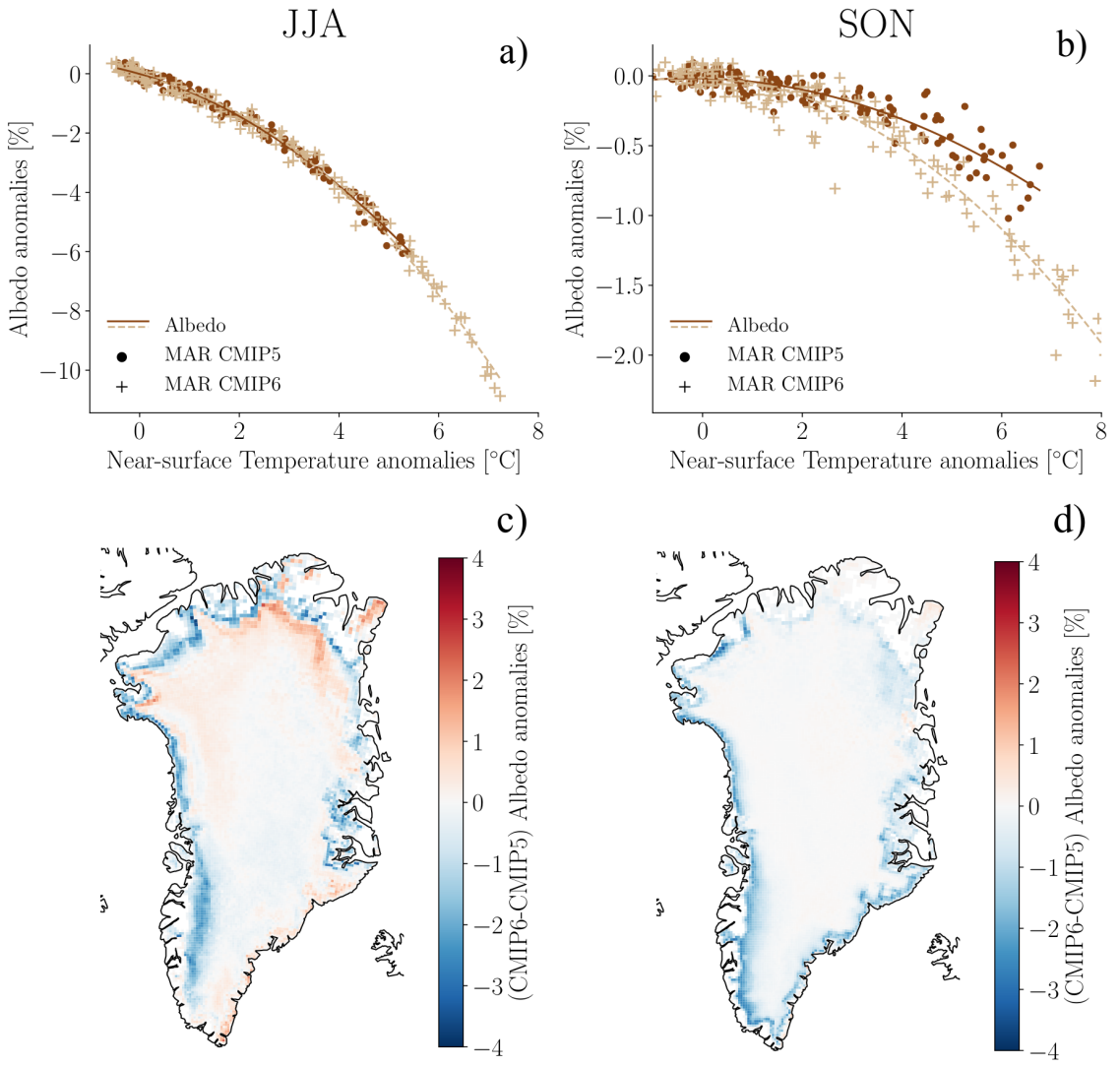

Figure 4.7: Albedo anomalies [%] according to near-surface air temperature anomalies [°C]] over GrIS and spatial distribution for a warming period of 4°C. Seasonal albedo anomalies according to seasonal near-surface temperature [°C] (top), and spatially distributed difference in change over GrIS for 4°C warming (bottom) for summer season (JJA) (left) and autumn season (SON) (right). For the spatial maps, areas of positive values (red colours) indicate higher values of albedo, and negative values indicate lower values of albedo in MAR CMIP6 when compared to MAR CMIP5. Regression equation and R^2 score can be found in Table B.2 in Appendix B.

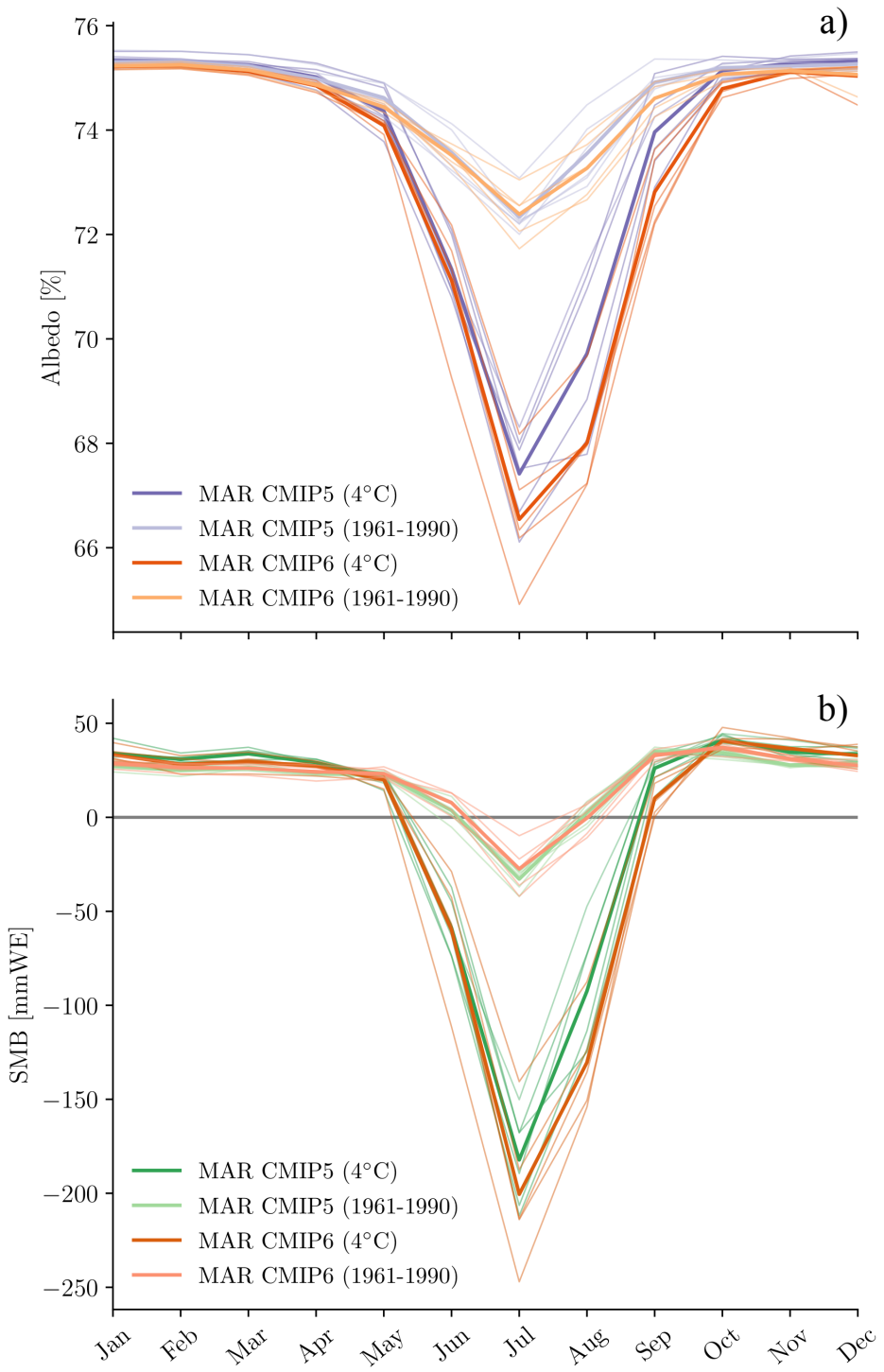

Figure 4.8: Annual cycle of Albedo and SMB. a) Annual Albedo cycle [%] from MAR CMIP5 (lavender/purple) and MAR CMIP6 (orange/red) for a thirty-year reference period (1961–1990) and a twenty-year (4°C ± 10 years) warming period. Thicker lines indicate the mean of MAR CMIP5 and MAR CMIP6 simulations, whereas the thinner lines indicate each individual model simulation. If the SMB is above the grey (i.e. SMB > 0) the ice sheet is gaining surface mass, and if it is below (i.e. SMB>0) it is losing more mass than it is gaining. **b)** Same as **a)**, but for SMB [mmWE] with MAR CMIP5 (mint/green) and MAR CMIP6 (orange/brown).

CHAPTER 5

Discussion

In this chapter we provide a discussion of the central findings of this thesis in Section 5.1, before we in Section 5.2 reflect on the changed cloud representation over Greenland in CMIP6. Lastly, we discuss some limitations of this study in Section 5.3.

5.1 Cloud induced SMB change in CMIP6

Higher melt and runoff rates, and subsequent greater surface mass loss in MAR CMIP6 can partly be explained by a greater warming by the end of the 21st century when compared to MAR CMIP5. We found a +1.4°C higher annual near-surface warming from the MAR CMIP6 model ensemble compared to MAR CMIP5. This is in line with the findings of Hofer et al., 2020, where they projected a difference in near-surface temperature anomaly of +1.3°C between high-emission scenario from the full CMIP6 model ensemble and the full CMIP5 model ensemble over the whole Arctic region, giving rise to a more pronounced GrIS mass loss in CMIP6 projections.

Moreover, from our projection of annual SMB change we found a stronger decrease in MAR CMIP6 compared to MAR CMIP5 even for a given near-surface temperature increase. Such a comparison between CMIP5 and CMIP6 over Greenland for a given warming has not been investigated in detail previous to this study. Our results suggest that parts of the greater mass loss in CMIP6 over the GrIS are driven by a difference in SMB sensitivity. We show that a change in cloud cover in MAR CMIP6, in the form of reduced cloud cover in summer and autumn, drives changes in the SEB that lead to excess melt at a given warming. This includes a more active ablation zone in summer and autumn from increased absorption of shortwave (SW) radiation and surface melt.

Our data of cloud projections over the GrIS show a reduction in cloud cover in both summer and autumn for MAR CMIP6 for a given near-surface temperature increase, the opposite of the cloud cover increase with warming in MAR CMIP5 (Figure 4.2 c and d). The spatial projections of ∼4°C revealed a homogeneous pattern of cloud cover change coming from changes in the upper level clouds (Figure 4.4). As explained in the background theory in Section 2.2 we expect a reduction in cloud cover to increase the amount of downwelling SW radiation reaching the surface, and reduce the downwelling longwave (LW) radiation, in line with our presented results. We also expect increase in the SW radiative energy fluxes to have the most impact over the darker ablation zone, and the reduction in LW radiative energy over the more reflective accumulation zone. Despite decreasing cloud cover in MAR CMIP6, there was no difference in the projections of COD in summer (Figure 4.3 a), suggesting the difference in SEB in summer comes from the difference in cloud cover alone. Conversely, a slightly more positive COD was found in MAR CMIP6 with warming in autumn compared to MAR CMIP5 (Figure 4.3 b). This could explain why we saw no difference in the SEB over the GrIS in autumn (Figure 4.2 b), where the effect of reduced cloud cover is compensated by the clouds getting more optically thick, and therefore no overall change in transmissivity and emissivity.

Our overall impression of the analysis over Greenland in summer is that we can see no spatially averaged difference in the SMB between MAR CMIP5 and MAR CMIP6 (Figure 4.1 b) because of

competing mechanisms between more positive melt and runoff in the lower ablation zone, and more positive refreezing and negative runoff anomalies in the percolation zone (Figure 4.6, left). This effect is induced by a reduction in the LW radiative energy, decelerating the removal of snow over the upper ablation zone and over the percolation zone. This is also supported by our analysis of the albedo over the ice sheet, where we saw a higher albedo over the percolation zone in MAR CMIP6, indicating a delayed removal of snow leading to more reflection of the incoming SW radiation compared to MAR CMIP5 (Figure 4.7 c). Additionally, clearer skies are also associated with cooler nights, and meltwater can then more easily refreeze - this is important in the percolation zone where meltwater is stored more readily in MAR CMIP6, limiting the bare ice exposure in this area.

However, there is a more sensitive melt-albedo feedback in the outer ablation zone where bare ice is exposed in MAR CMIP6. Here, the reduction in cloud cover allows more net SW to be absorbed, leading to more melt which in turn leads to enhanced darkening and allowing for further absorption of SW radiation (Figure 4.5 b and Figure 4.7 d). We observe similar competing effects between melt and refreezing in the ablation zone as discussed by van den Broeke et al., 2008b. During melt events (2003 – 2007) they found an exponential increase in total melt and runoff towards the ice sheet margin. In the upper ablation zone, about 40% of the melt energy was consumed by refreezing of the meltwater, where closer to the tundra they observed continuous melt during melt season due to little accumulation of winter snow over the bare ice.

In our study, parts of the higher refreezing in the percolation zone in MAR CMIP6 can potentially be explained by the faster warming pace of the CMIP6 ensemble (Figure 3.2). Different warming rates imply that for the selection of the twenty-year period of $\sim$4°C warming, the models that warm faster have not had time to fully extend the ablation zone to higher elevations to the same extent as other models that reach the same atmospheric temperature at a later stage. In the "slower" models the ablation zone is more in equilibrium with the warming climate and therefore likely already larger in CMIP5 than in CMIP6 at a given warming, because CMIP6 generally warms faster. This could explain parts of the higher refreezing in the percolation zone, because CMIP5 might already have gotten rid of the buffering snow layer there.

The masking of competing effects between the ablation zone and the percolation zone when looking at spatially averaged projections highlights the value of investigating spatial map projections over the GrIS to capture spatial differences. This also demonstrates, as previously stated (Chapter 3 Section 3.1), the need for high enough resolution for projections of the GrIS climate and SMB to sufficiently capture the surface dynamics in the ablation and percolation zones.

5.2 Change in cloud representation over Greenland

Through the work of our thesis we suggest a change in cloud representation in CMIP6 to be the main driver of the stronger SMB loss from the GrIS for a given warming in CMIP6 compared to CMIP5. However, possible drivers of the observed difference between the projections of cloud cover and COD between MAR CMIP5 and MAR CMIP6 have not been covered in the analysis. We suggest that future studies look in more detail at the circulation in both CMIP5 and CMIP6 over Greenland, although initial analysis suggest no notable difference between the two ensembles (Delhasse et al., 2020).

Because all simulations are run with the same regional climate model setup throughout this study we believe that the difference in the cloud cover response with warming stems from the GCMs used to force the regional climate model MAR. This would be in line with recent results showing that changes in cloud physics between CMIP5 and CMIP6 have lead to a greater climate sensitivity in CMIP6 (Zelinka et al., 2020).

Our data also showed a decrease in the upper level cloud cover in MAR CMIP6 with increasing near-surface temperature levels, whereas MAR CMIP5 showed increasing cloud cover with warming. Through spatial map projection, we found a homogeneous pattern when comparing the different cloud cover responses over the GrIS between MAR CMIP6 and MAR CMIP5 (Figure 4.4). We

argue that this difference in cloud cover is not circulation-driven, as we would expect this to result in a more distinct spatial pattern. This is also as expected from the findings of Hanna et al., 2018 and Delhasse et al., 2021 where they detected no future circulation changes over Greenland from the CMIP5 and CMIP6 GCMs respectively.

In our results, we also found a similar projection in COD between the two model ensembles, even with decreasing cloud cover in MAR CMIP6. One reason for the concurrent increase in COD simultaneously with decreasing cloud cover could be that these changes in cloud properties happen at different altitude. From our data the cloud cover decreased for high level clouds. We suspect the optical thickness to increase at a different level than the high clouds. We compare the two model ensembles for a given near-surface temperature increase, however the projections from CMIP5 and CMIP6 might differ in the vertical temperature gradient (lapse rate) which could impact the COD. The exact differences in temperature and humidity should be explored at different vertical levels to gain better understanding of the differences between CMIP6 and CMIP5, however because of data limitations and time constrains this has not been investigated in our analysis.

5.3 Limitations

In this final section we will discuss some limitations of this study.

The projections of climate variable anomalies for a given temperature increase are fitted with a regression line to the modelled data. In obtaining a more robust projection of these regression lines, we could have calculated a confidence interval for the regression coefficient and compared multiple possible fits for the regression. Furthermore, the spatial anomaly plots should have been accompanied with evaluation of significance in each grid point.

In our analysis we use simulation outputs from MAR which use a fixed ice sheet topography throughout the simulations. A fixed ice sheet extent will underestimate future projections of feedbacks from changes in the ice sheet extent, shape and elevation. However, in a previous study by coupling MAR to a 3-D ice sheet model to account for ice-sheet interactions, Le Clec'h et al., 2019 found a 9.3% lower sea-level contribution from the GrIS in 2150 in a experiment with no feedback compared to a experiment with parameterized SMB-elevation feedback. They suggested that the effect of different feedbacks is amplified over time. Therefore we suggest that by 2100 elevation feedbacks plays a minor role, however the effect of these feedbacks will become more important as warming and mass loss progresses after 2100.

The five GCMs composing the MAR CMIP6 model ensemble of our study are representative of the mean temporal temperature projections until 2100 (Hofer et al., 2020, Figure 1) for the total model ensemble of CMIP6 models. However, in this study we have not carried out any assessment of how other climate parameters within our model ensembles compare to the full range ensembles of CMIP6 models. Therefore, we cannot draw any conclusions to how our five-model ensembles represent the full spread. However, this would be interesting to investigate in further work.

CHAPTER 6

Conclusion

In this final chapter we conclude the thesis with a summary of our main findings in Section 6.1, and provide suggestions for further research in Section 6.2.

6.1 Summary

We performed an analysis of high-resolution regional climate model simulations over the GrIS to investigate possible physical mechanisms driving the excess SMB loss in CMIP6 models. Previous to this study, it was believed that the excess SMB reduction seen in CMIP6 compared to CMIP5 was solely a product of a greater Arctic amplification signal in CMIP6 models. Our work suggests that parts of the greater mass loss in CMIP6 over the GrIS is driven by a difference in SMB sensitivity, from a change in cloud representation in CMIP6 models.

By comparing two model ensembles of six CMIP5 RCP8.5 and five CMIP6 SSP5-8.5 future projections for a given temperature increase, we found a greater sensitivity of Greenland surface mass loss in CMIP6 centered around summer and autumn. Yet, the difference in mass loss between CMIP5 and CMIP6 was largest during autumn.

Assessment of future changes in the SEB and cloud properties over the GrIS suggested a reduction in high clouds during summer and autumn to be the main driver of additional SW radiation reaching the surface, while cloud cover increases with warming in CMIP5. However, the detailed mechanisms behind different cloud cover trends with warming in CMIP6 compared to CMIP5 are still unanswered.

Our data showed a stronger melt-albedo feedback in CMIP6 mainly in the lower ablation zone where bare ice is continuously exposed during summer and early autumn. Here we observed more surface melt and darkening of the surface during summer, from an increase in SWD from reduced cloud cover. However, because of a competing mechanism in the percolation zone leading to more refreezing, there was no difference in the total SMB projection between CMIP5 and CMIP6 in summer. In the autumn however, there was a stronger melt and runoff signal in CMIP6 from the darkening of the lower albedo zone in summer.

Our analysis highlights that Greenland is loosing more mass in CMIP6 due to two factors;

1) a (known) greater sensitivity to GHG emissions and therefore warmer temperatures
2) previously undocumented cloud-related surface energy budget changes between CMIP5 and CMIP6 that enhance the GrIS sensitivity to warming.

6.2 Further research

Time constraints limits the extent of the research in a Master's thesis, consequently the research of this thesis is far from complete. Nevertheless, several ideas have evolved through our work, and we will end by presenting some of the ideas for further research.

As previously discussed in Chapter 5, our study did not assess how the five-model ensemble of CMIP6 models compare to the the full CMIP6 model ensemble for climate variables other than near-surface warming. Thus, this would be a natural next step to further investigate how our results apply to the whole CMIP6 range.

Additionally, a question that is still unanswered is why our results showed decreasing cloud cover simultaneously with increasing COD. For this matter we suggest looking into the exact difference in temperature and humidity at different vertical levels in CMIP6. This could give us a pinpoint to where the observed cloud properties originate, and what causes them.

A focus on the differences in anomalies between CMIP5 and CMIP6 was maintained throughout our study. However, the impact of absolute contribution to future sea-level rise from excess meltwater runoff is also of immediate concern. Further understanding of the global impact of cloud cover change on the SMB over the GrIS in CMIP6 could be explored by investigating the correlation between absolute SMB changes and their connection to cloud properties.

In our study, we focused on the differences between CMIP5 and CMIP6 model projections over Greenland. Moreover, given the spatial extent of Greenland our findings give us reason to believe that differences between CMIP5 and CMIP6 projections would also be expected for a given warming over other parts of the Arctic, which we think should be investigated in future studies.

Appendices

APPENDIX A

Figures

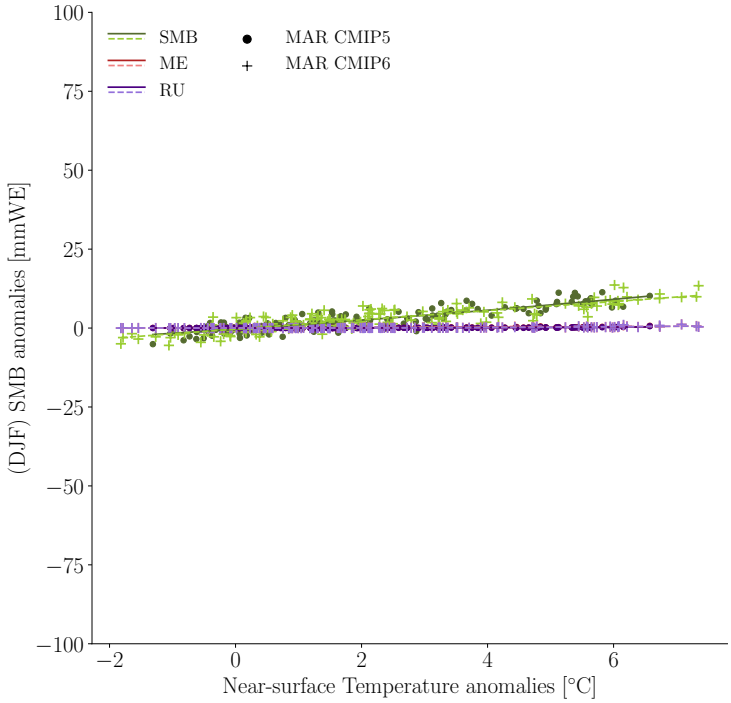

Figure A.1: Seasonal SMB, melt and runoff anomalies [mmWE] over the GrIS according to near-surface temperature anomalies [°C]. Winter (DJF) SMB-, melt- (ME), and runoff anomalies (RU) [mmWE] over the GrIS as a function of annual near-surface temperature anomalies [°C] from MAR CMIP5 (dots) and MAR CMIP6 (crosses), with regression drawn in solid lines for MAR CMIP5 and scattered lines for MAR CMIP6. All anomalies are related to the thirty-years averaged reference period (1961–1990). Regression equation and R^2 score can be found in Table B.2.

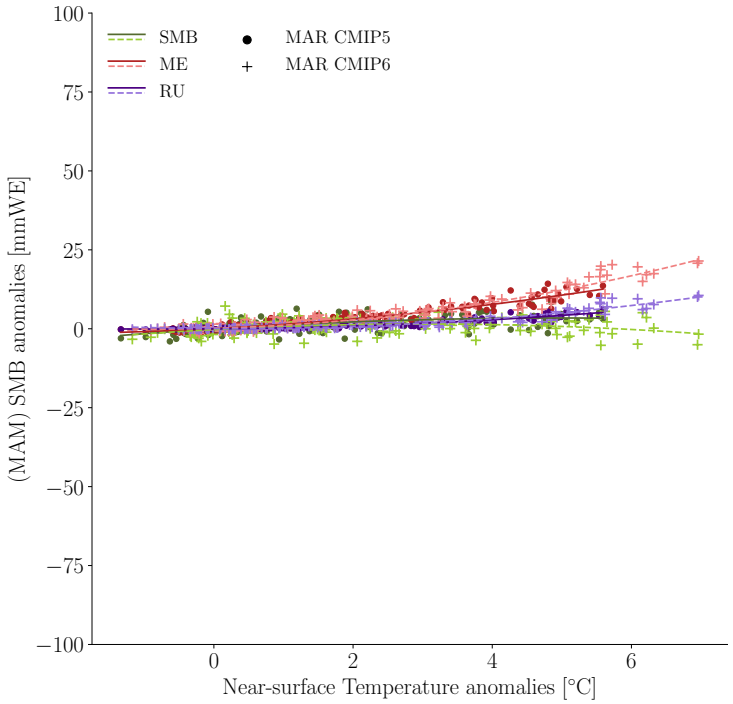

Figure A.2: Seasonal SMB, melt and runoff anomalies [mmWE] over the GrIS according to near-surface temperature anomalies [°C]. spring (MAM) SMB, melt (ME), and runoff anomalies (RU) [mmWE] over the GrIS as a function of annual near-surface temperature anomalies [°C] from MAR CMIP5 (dots) and MAR CMIP6 (crosses), with regression drawn in solid lines for MAR CMIP5 and scattered lines for MAR CMIP6. All anomalies are related to the thirty-years averaged reference period (1961–1990).

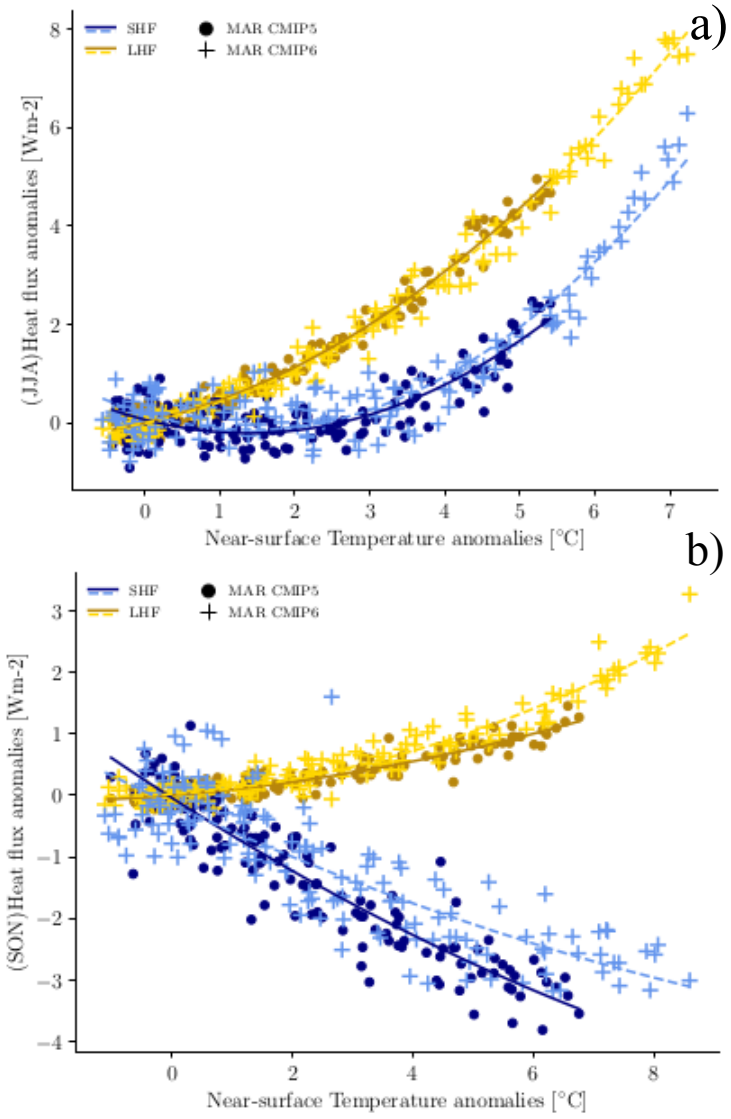

Figure A.3: Seasonal heat flux anomalies according [Wm^{-2}] to seasonal near-surface anomalies [°C]. a) summer seasonal (JJA) heat flux anomalies according to summer seasonal near-surface temperature anomalies from MAR CMIP5 (dots) and MAR CMIP6 (crosses), with regression drawn in solid lines for MAR CMIP5 and scattered lines for MAR CMIP6. All anomalies are related to the thirty-years average reference period (1961–1990). Positive values indicate flux towards the surface. **b)** same as **a)**, but for autumn season.

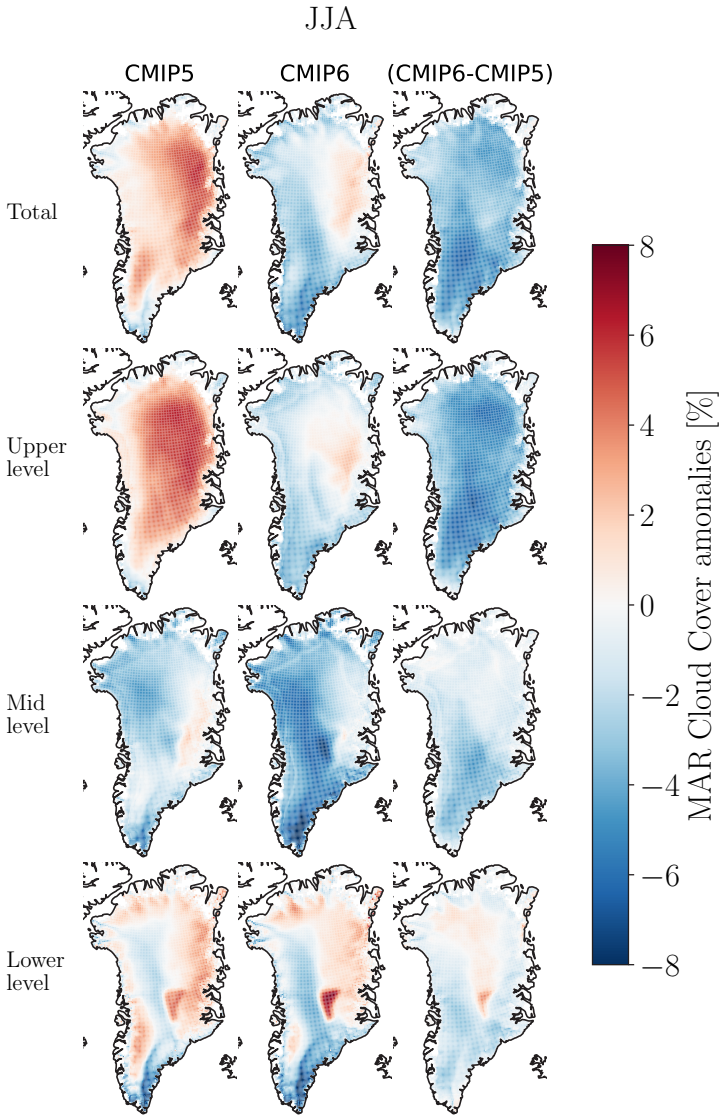

Figure A.4: Spatial projection of Cloud cover anomalies [%] for MAR CMIP5 and MAR CMIP6 simulations (+ 4 °C ± 10 years) for summer (JJA). Twenty-year average (4 °C ± 10 years) of the cloud cover [%] over the GrIS) for summer (JJA). The four rows from top-down indicate the total, upper level, mid level, and lower level cloud cover. The three columns from left to right indicate the cloud cover anomalies for MAR CMIP5, for MAR CMIP6, and for the difference between the two (CMIP6-CMIP5). For MAR CMIP5 and MAR CMIP6 a positive value (red) indicates an increase in cloud cover, and a negative value (blue) a reduction in cloud cover compared to the reference period. For the difference (CMIP6-CMIP5) a positive value (red) indicates more positive cloud cover anomaly, and negative values (blue) indicate a more negative cloud cover anomaly in MAR CMIP6 compared to MAR CMIP5.

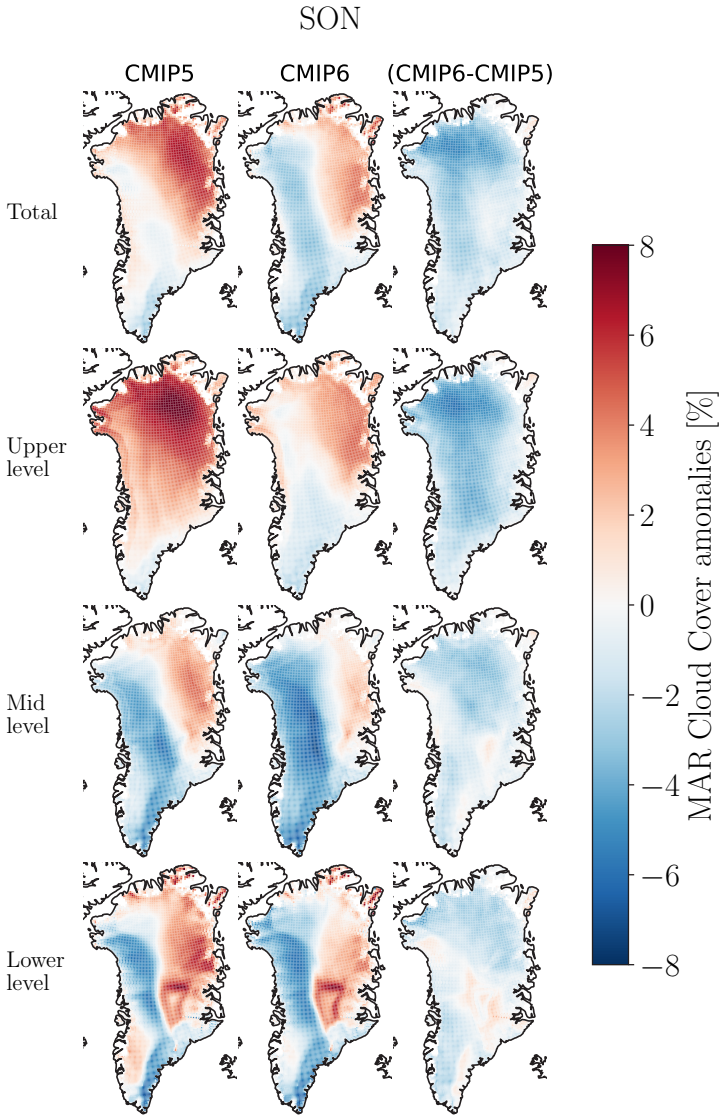

Figure A.5: Spatial projection of Cloud cover anomalies [%] for MAR CMIP5 and MAR CMIP6 simulations (+ 4 °C ± 10 years) for autumn (SON). Twenty-year average (4 °C ± 10 years) of the cloud cover [%] over the GrIS) for autumn (SON). The four rows from top-down indicate the total, upper level, mid level, and lower level cloud cover. The three columns from left to right indicate the cloud cover anomalies for MAR CMIP5, for MAR CMIP6, and for the difference between the two (CMIP6-CMIP5). For MAR CMIP5 and MAR CMIP6 a positive value (red) indicates an increase in cloud cover, and a negative value (blue) a reduction in cloud cover compared to the reference period. For the difference (CMIP6-CMIP5) a positive value (red) indicates more positive cloud cover anomaly, and negative values (blue) indicate a more negative cloud cover anomaly in MAR CMIP6 compared to MAR CMIP5.

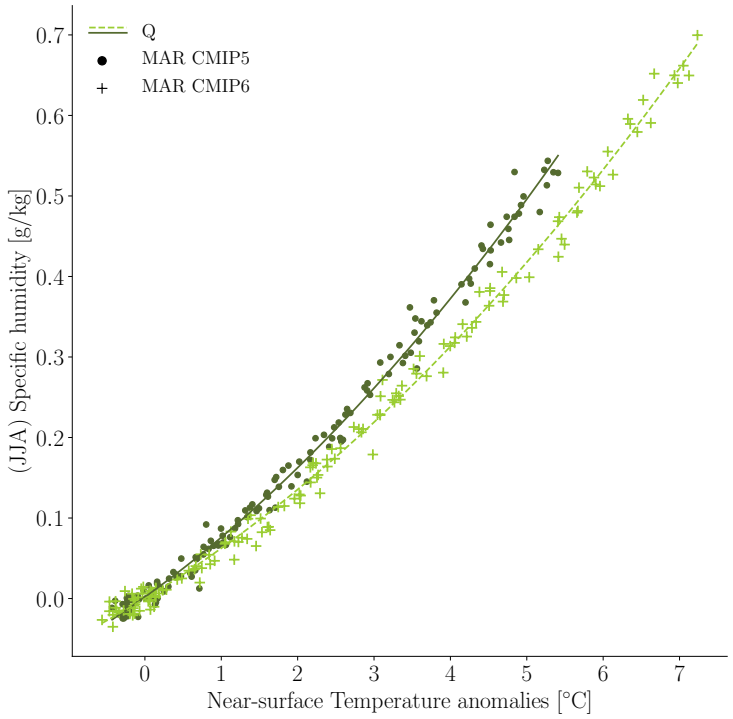

Figure A.6: Summer (JJA) specific humidity [gkg^{-}] according to near-surface temperature anomalies [°C]. Summer (JJA) specific humidity (Q) anomalies [gkg^{-}] as a function of seasonal near-surface anomalies [°C] from MAR CMIP5 (dots) and MAR CMIP6 (crosses), with regression drawn in solid lines for MAR CMIP5 and scattered lines for MAR CMIP6. All anomalies are related to the thirty-years average reference period (1961–1990). Positive values indicate flux towards the surface. Regression equation and R^2 score can be found in Table B.2.

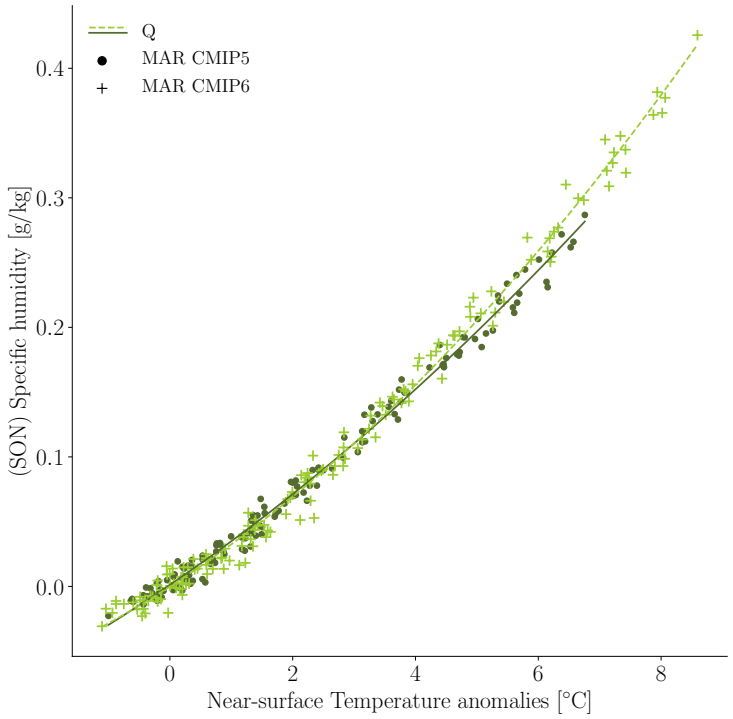

Figure A.7: Autumn (SON) specific humidity [gkg^{-}] according to near-surface temperature anomalies [°C]. Autumn (SON) specific humidity (Q) anomalies [gkg^{-}] as a function of seasonal near-surface anomalies [°C] from MAR CMIP5 (dots) and MAR CMIP6 (crosses), with regression drawn in solid lines for MAR CMIP5 and scattered lines for MAR CMIP6. All anomalies are related to the thirty-years average reference period (1961–1990). Positive values indicate flux towards the surface. Regression equation and R^2 score can be found in Table B.2.

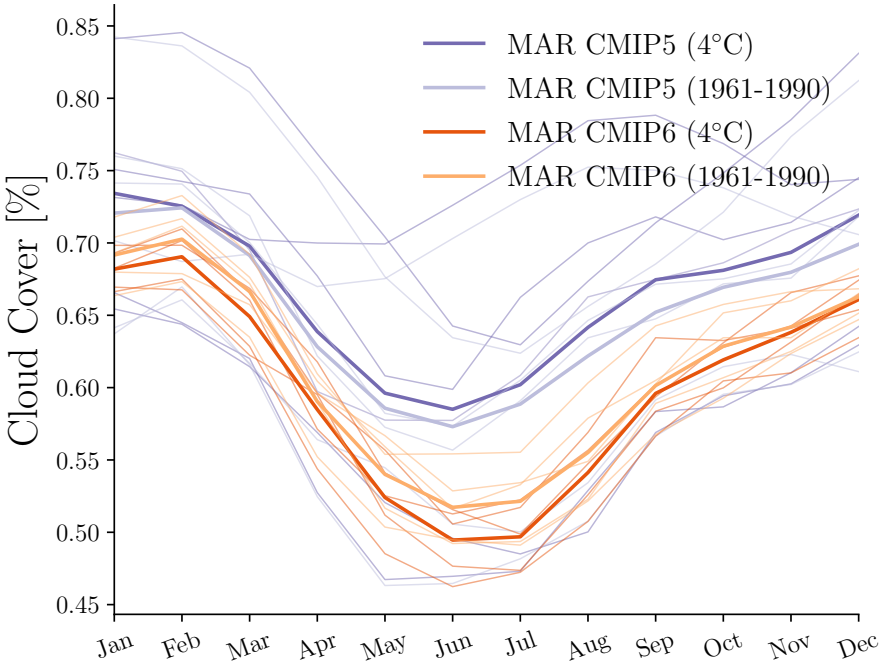

Figure A.8: Annual cycle of Cloud Cover. Annual Cloud cover [%] cycle from MAR CMIP5 (lavender/purple) and MAR CMIP6 (orange/red) for a thirty-year reference period (1961–1990) and a twenty-year (4°C ± 10 years) warming period. Thicker lines indicate the mean of MAR CMIP5 and MAR CMIP6 simulations, whereas the thinner lines indicate each individual model simulation.

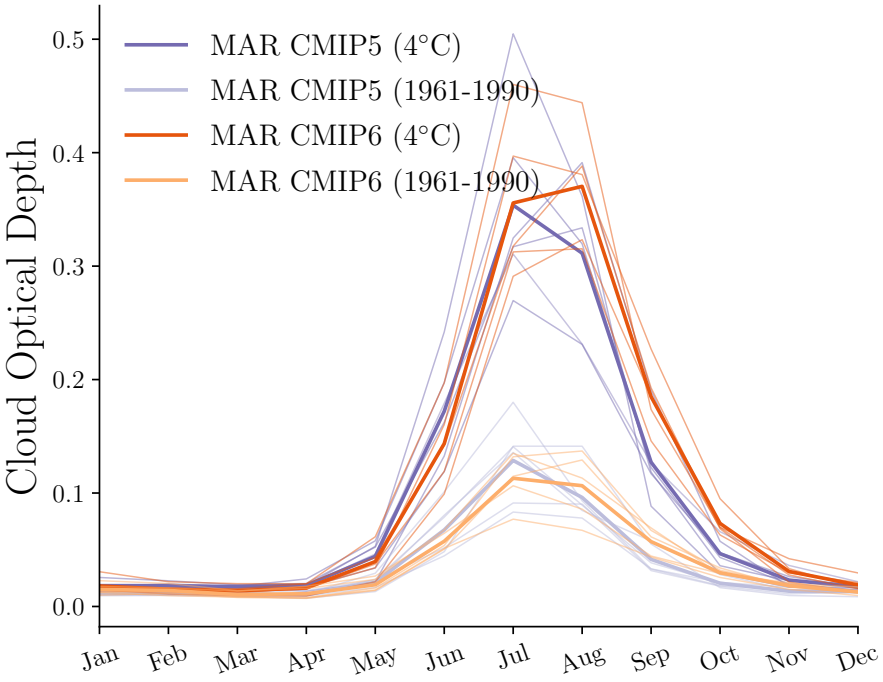

Figure A.9: Annual cycle of Cloud Optical Depth. Annual COD cycle from MAR CMIP5 (lavender/purple) and MAR CMIP6 (orange/red) for a thirty-year reference period (1961–1990) and a twenty-year (4°C ± 10 years) warming period. Thicker lines indicate the mean of MAR CMIP5 and MAR CMIP6 simulations, whereas the thinner lines indicate each individual model simulation.

APPENDIX B

Tables

Climate variable	Abbreviation	Unit
Albedo	ALB	-
Cloud Cover	CC	-
Cloud Optical Depth	COD	-
Latent heat flux	LHF	Wm^{-2}
Longwave radiation (down)	LWD	Wm^{-2}
Longwave radiation (net)	LW_{net}	Wm^{-2}
Longwave radiation (up)	LWU	Wm^{-2}
Melt	ME	mmWE
Net radiative flux	-	Wm^{-2}
Refreezing	RZ	mmWE
Runoff	RU	mmWE
Sensible heat flux	SHF	Wm^{-2}
Shortwave radiation (down)	SWD	Wm^{-2}
Shortwave radiation (net)	SW_{net}	Wm^{-2}
Specific humidity	Q	gkg^{-}
Surface Mass Balance	SMB	mmWE

Table B.1: Overview of all climate variables used in this thesis with corresponding abbreviation and unit.

	JJA		SON	
Variable	Regression Function	R^2 score	Regression Function	R^2 score
ALB				
CMIP5	f(x)= -0.12 x^2 + -0.48 x + -0.01	0.990	f(x)= -0.02 x^2 + -0.01 x + -0.02	0.852
CMIP6	f(x)= -0.15 x^2 + -0.35 x + -0.08	0.991	f(x)= -0.03 x^2 + -0.01 x + -0.01	0.945
CC				
CMIP5	f(x)= 0.04 x^2 + 0.26 x + -0.15	0.418	f(x)= 0.03 x^2 + 0.24 x + -0.05	0.566
CMIP6	f(x)= -0.04 x^2 + -0.13 x + -0.39	0.333	f(x)= 0.01 x^2 + -0.15 x + 0.12	0.081
COD				
CMIP5	f(x)= 0.01 x^2 + 0.02 x + -0.01	0.980	f(x)= 0.001 x^2 + 0.0046 x + 0.0002	0.958
CMIP6	f(x)= 0.01 x^2 + 0.02 x + 0.01	0.986	f(x)= 0.002 x^2 + 0.0041 x + 0.0008	0.977
LHF [Wm^{-2}]				
CMIP5	f(x)= 0.1 x^2 + 0.36 x + 0.01	0.980	f(x)= 0.01 x^2 + 0.08 x + 0.01	0.866
CMIP6	f(x)= 0.11 x^2 + 0.32 x + -0.01	0.986	f(x)= 0.03 x^2 + 0.06 x + 0.02	0.931
LW_{net} [Wm^{-2}]				
CMIP5	f(x)= 0.09 x^2 + 0.79 x + -0.02	0.860	f(x)= -0.02 x^2 + 0.52 x + 0.01	0.777
CMIP6	f(x)= 0.09 x^2 + 0.35 x + -0.18	0.794	f(x)= -0.01 x^2 + 0.22 x + 0.08	0.355
LWD [Wm^{-2}]				
CMIP5	f(x)= 0.07 x^2 + 5.06 x + -0.05	0.989	f(x)= -0.0 x^2 + 4.18 x + 0.02	0.996
CMIP6	f(x)= 0.07 x^2 + 4.64 x + -0.2	0.992	f(x)= 0.03 x^2 + 3.84 x + 0.17	0.994
LWU [Wm^{-2}]				
CMIP5	f(x)= 0.02 x^2 + -4.28 x + 0.02	1.0	f(x)= -0.02 x^2 + -3.66 x + -0.01	1.0
CMIP6	f(x)= 0.03 x^2 + -4.26 x + 0.07	1.0	f(x)= -0.02 x^2 + -3.63 x + -0.05	1.0
ME [mmWE]				
CMIP5	f(x)= 4.02 x^2 + 18.31 x + -0.19	0.997	f(x)= 0.22 x^2 + 0.59 x + 0.07	0.939
CMIP6	f(x)= 5.14 x^2 + 13.25 x + 1.06	0.996	f(x)= 0.46 x^2 + 0.3 x + 0.23	0.960
Net_{rad} [Wm^{-2}]				
CMIP5	f(x)= 0.28 x^2 + 1.54 x + -0.08	0.995	f(x)= -0.01 x^2 + 0.49 x + 0.02	0.827
CMIP6	f(x)= 0.38 x^2 + 1.02 x + -0.08	0.991	f(x)= 0.01 x^2 + 0.24 x + 0.03	0.619
RU [mmWE]				
CMIP5	f(x)= 4.34 x^2 + 12.43 x + 0.24	0.995	f(x)= 0.34 x^2 + 0.57 x + 0.13	0.948
CMIP6	f(x)= 5.53 x^2 + 6.63 x + 1.60	0.993	f(x)= 0.66 x^2 + 0.15 x + 0.34	0.966
SMB [mmWE]				
CMIP5	f(x)= -4.11 x^2 + -9.73 x + -0.38	0.991	f(x)= -0.26 x^2 + 1.52 x + -0.24	0.153
CMIP6	f(x)= -5.38 x^2 + -4.42 x + -2.33	0.990	f(x)= -0.59 x^2 + 1.88 x + -0.18	0.777
SHF [Wm^{-2}]				
CMIP5	f(x)= 0.14 x^2 + -0.40 x + 0.07	0.697	f(x)= 0.02 x^2 + -0.63 x + -0.04	0.856
CMIP6	f(x)= 0.16 x^2 + -0.46 x + 0.19	0.894	f(x)= 0.01 x^2 + -0.45 x + -0.14	0.711
SW_{net} [Wm^{-2}]				
CMIP5	f(x)= 0.19 x^2 + 0.76 x + -0.05	0.927	f(x)= 0.01 x^2 + -0.04 x + 0.01	0.149
CMIP6	f(x)= 0.29 x^2 + 0.67 x + 0.1	0.946	f(x)= 0.01 x^2 + 0.02 x + -0.05	0.543
SWD [Wm^{-2}]				
CMIP5	f(x)= -0.26 x^2 + -2.38 x + -0.29	0.896	f(x)= -0.01 x^2 + -0.30 x + -0.03	0.734
CMIP6	f(x)= -0.17 x^2 + -1.68 x + -0.04	0.895	f(x)= -0.03 x^2 + -0.09 x + -0.28	0.559

Table B.2: Function f(x) = ax^2 + bx + c for fitted regression line from observed data points of climate variables, and R^2 score for the corresponding regression line for all climate variable projections of summer (JJA, left) and autumn (SON, right) used in the analysis of this thesis.

APPENDIX C

Computer Code

The computer code for the analysis done for the work of this thesis can be accessed at https://github.com/idunnam/Thesis.

Bibliography

AMS, A. M. S. (2012). *Optical thickness, Glossary of Meteorology*. URL: https://glossary.ametsoc.org/wiki/Optical_thickness (visited on 08/01/2021).

Arias, P. A. et al. (2021). 'Technical Summary'. In: *Climate Change 2021: The Physical Science Basis. Contribution of Working Group I to the Sixth Assessment Report of the Intergovernmental Panel on Climate Change*. Ed. by Masson-Delmotte, V. et al. Cambridge University Press.

Barthel, A., Agosta, C., Little, C. M., Hattermann, T., Jourdain, N. C., Goelzer, H., Nowicki, S., Seroussi, H., Straneo, F. and Bracegirdle, T. J. (2020). 'CMIP5 model selection for ISMIP6 ice sheet model forcing: Greenland and Antarctica'. In: *The Cryosphere* vol. 14, no. 3, pp. 855–879.

Box, J., Fettweis, X., Stroeve, J., Tedesco, M., Hall, D. and Steffen, K. (2012). 'Greenland ice sheet albedo feedback: Thermodynamics and atmospheric drivers'. eng. In: *The cryosphere* vol. 6, no. 4, pp. 821–839.

Broeke, M. van den, Smeets, P., Ettema, J. and Munneke, P. K. (2008a). 'Surface radiation balance in the ablation zone of the west Greenland ice sheet'. eng. In: *Journal of Geophysical Research: Atmospheres* vol. 113, no. D13, D13105–n/a.

Brun, E., David, P., Sudul, M. and Brunot, G. (1992). 'A numerical model to simulate snow-cover stratigraphy for operational avalanche forecasting'. In: *Journal of Glaciology* vol. 38, no. 128, pp. 13–22.

Chen, D. et al. (2021). 'Framing, Context, and Methods'. In: *Climate Change 2021: The Physical Science Basis. Contribution of Working Group I to the Sixth Assessment Report of the Intergovernmental Panel on Climate Change*. Ed. by Masson-Delmotte, V. et al. Cambridge University Press.

De Ridder, K. (1998). 'The Impact of Vegetation Cover on Sahelian Drought Persistence'. eng. In: *Boundary-layer meteorology* vol. 88, no. 2, pp. 307–321.

Delhasse, A., Fettweis, X., Kittel, C., Amory, C. and Agosta, C. (2018). 'Brief communication: Impact of the recent atmospheric circulation change in summer on the future surface mass balance of the Greenland ice sheet'. eng. In: *The cryosphere discussions*, pp. 1–13.

Delhasse, A., Hanna, E., Kittel, C. and Fettweis, X. (2021). 'Brief communication: CMIP6 does not suggest any atmospheric blocking increase in summer over Greenland by 2100'. eng. In: *International journal of climatology* vol. 41, no. 4, pp. 2589–2596.

Delhasse, A., Kittel, C., Amory, C., Hofer, S., Van As, D., Fausto, R. and Fettweis, X. (2020). 'Brief communication: Evaluation of the near-surface climate in ERA5 over the Greenland Ice Sheet'. eng. In: *The cryosphere* vol. 14, no. 3, pp. 957–965.

Devore, J. L. and Berk, K. N. (2018). *Modern Mathematical Statistics with Applications*. eng. Second Edition. Springer Texts in Statistics. New York, NY: Springer New York.

Dickinson, R. E., Errico, R. M., Giorgi, F. and Bates, G. T. (1989). 'A regional climate model for the western United States'. eng. In: *Climatic change* vol. 15, no. 3, pp. 383–422.

Doblas-Reyes, F. J. et al. (2021). 'Linking Global to Regional Climate Change'. In: *Climate Change 2021: The Physical Science Basis. Contribution of Working Group I to the Sixth Assessment Report of the Intergovernmental Panel on Climate Change*. Ed. by Masson-Delmotte, V. et al. Cambridge University Press.

Enderlin, E. M., Howat, I. M., Jeong, S., Noh, M.-J., Angelen, J. H. van and Broeke, M. R. van den (2014). 'An improved mass budget for the Greenland ice sheet'. eng. In: *Geophysical research letters* vol. 41, no. 3, pp. 866–872.

Eyring, V. et al. (2021). 'Human Influence on the Climate System'. In: *Climate Change 2021: The Physical Science Basis. Contribution of Working Group I to the Sixth Assessment Report of the Intergovernmental Panel on Climate Change*. Ed. by Masson-Delmotte, V. et al. Cambridge University Press.

Fettweis, X., Franco, B., Tedesco, M., Angelen, J. van, Lenaerts, J., Broeke, M. van den and Gallee, H. (2013a). 'Estimating the Greenland ice sheet surface mass balance contribution to future sea level rise using the regional atmospheric climate model MAR'. eng. In: *The cryosphere* vol. 7, no. 2, pp. 469–489.

Fettweis, X., Hanna, E., Lang, C., Belleflamme, A., Erpicum, M. and Gallée, H. (2013b). 'Brief communication Important role of the mid-tropospheric atmospheric circulation in the recent surface melt increase over the Greenland ice sheet'. eng. In: *The cryosphere* vol. 7, no. 1, pp. 241–248.

Fettweis, X., Tedesco, M., Broeke, M. van den and Ettema, J. (2011). 'Melting trends over the Greenland ice sheet (1958–2009) from spaceborne microwave data and regional climate models'. eng. In: *The cryosphere* vol. 5, no. 2, pp. 359–375.

Fettweis, X., Gallée, H., Lefebre, F. and Ypersele, J.-P. van (2005). 'Greenland surface mass balance simulated by a regional climate model and comparison with satellite-derived data in 1990–1991'. eng. In: *Climate dynamics* vol. 24, no. 6, pp. 623–640.

Fettweis, X., Hofer, S., Krebs-Kanzow, U., Amory, C., Aoki, T., Berends, C. J., Born, A., Box, J. E. and Wouters, B. (2020). 'GrSMBMIP: Intercomparison of the modelled 1980-2012 surface mass balance over the Greenland Ice Sheet'. eng. In: *The cryosphere* vol. 14, no. 11, pp. 3935–3958.

Field, C.B. et al. (2014). *IPCC, 2014: Summary for policymakers. In: Climate Change 2014: Impacts, Adaptation, and Vulnerability. Part A: Global and Sectoral Aspects. Contribution of Working Group II to the Fifth Assessment Report of the Intergovernmental Panel on Climate Change*. Cambridge, United Kingdom and New York, NY, USA, pp. 1-32.

Fouquart, Y., Buriez, J. C., Herman, M. and Kandel, R. S. (1990). 'The influence of clouds on radiation: A climate-modeling perspective'. eng. In: *Reviews of geophysics (1985)* vol. 28, no. 2, pp. 145–166.

Fox-Kemper, B. et al. (2021). 'Ocean, Cryosphere, and Sea Level Change'. In: *Climate Change 2021: The Physical Science Basis. Contribution of Working Group I to the Sixth Assessment Report of the Intergovernmental Panel on Climate Change*. Ed. by Masson-Delmotte, V. et al. Cambridge University Press.

Gallée, H. (1995). 'Simulation of the Mesocyclonic Activity in the Ross Sea, Antarctica'. eng. In: *Monthly weather review* vol. 123, no. 7, pp. 2051–2069.

Gallée, H. and Schayes, G. (1994). 'Development of a three-dimensional meso-γ primitive equation model: katabatic winds simulation in the area of Terra Nova Bay, Antarctica'. eng. In: *Monthly weather review* vol. 122, no. 4, pp. 671–685.

Goelzer, H. et al. (2020). 'The future sea-level contribution of the Greenland ice sheet: A multi-model ensemble study of ISMIP6'. eng. In: *The cryosphere* vol. 14, no. 9, pp. 3071–3096.

Goosse, H. et al. (2018). 'Quantifying climate feedbacks in polar regions'. eng. In: *Nature communications* vol. 9, no. 1, pp. 1919–1919.

Hanna, E., Fettweis, X. and Hall, R. J. (2018). 'Recent changes in summer Greenland blocking captured by none of the CMIP5 models'. eng. In: *The cryosphere discussions*, pp. 1–8.

Hanna, E., Mernild, S. H., Cappelen, J. and Steffen, K. (2012). 'Recent warming in Greenland in a long-term instrumental (1881-2012) climatic context: I. Evaluation of surface air temperature records'. eng. In: *Environmental research letters* vol. 7, no. 4, pp. 45404–15.

Hofer, S., Lang, C., Amory, C., Kittel, C., Delhasse, A., Tedstone, A. and Fettweis, X. (2020). 'Greater Greenland Ice Sheet contribution to global sea level rise in CMIP6'. eng ; nor. In: *Nature communications* vol. 11, no. 1, pp. 6289–11.

Hofer, S., Tedstone, A. J., Fettweis, X. and Bamber, J. L. (2017). 'Decreasing cloud cover drives the recent mass loss on the Greenland Ice Sheet'. eng. In: *Science advances* vol. 3, no. 6, e1700584–e1700584.

Le Clec'h, S., Charbit, S., Quiquet, A., Fettweis, X., Dumas, C., Kageyama, M., Wyard, C. and Ritz, C. (2019). 'Assessment of the Greenland ice sheet-atmosphere feedbacks for the next century with a regional atmospheric model coupled to an ice sheet model'. eng. In: *The cryosphere* vol. 13, no. 1, pp. 373–395.

Lenaerts, J., Medley, B., Broeke, M. R. van den and Wouters, B. (2019). 'Observing and Modeling IceâSheet Surface Mass Balance'. eng. In: *Reviews of geophysics (1985)* vol. 57, no. 2, pp. 376–420.

Marshall, J. and Plumb, R. A. (2007). *Atmosphere, Ocean and Climate Dynamics: An Introductory Text*. eng. San Diego: Elsevier Science and Technology.

Meehl, G. A., Senior, C. A., Eyring, V., Flato, G., Lamarque, J.-F., Stouffer, R. J., Taylor, K. E. and Schlund, M. (2020). 'Context for interpreting equilibrium climate sensitivity and transient climate response from the CMIP6 Earth system models'. eng. In: *Science advances* vol. 6, no. 26, eaba1981–eaba1981.

Morlighem, M. et al. (2017). 'BedMachine v3: Complete Bed Topography and Ocean Bathymetry Mapping of Greenland From Multibeam Echo Sounding Combined With Mass Conservation'. eng. In: *Geophysical research letters* vol. 44, no. 21, pp. 11, 051–11, 061.

Morrison, H., Curry, J. and Khvorostyanov, V. (2005). 'A new double-moment microphysics parameterization for application in cloud and climate models. Part I: Description'. eng ; rus. In: *Journal of the atmospheric sciences* vol. 62, no. 6, pp. 1665–1677.

Noël, B., Berg, W. J. van de, Lhermitte, S. and Broeke, M. R. van den (2019). 'Rapid ablation zone expansion amplifies north Greenland mass loss'. eng. In: *Science advances* vol. 5, no. 9, eaaw0123.

O'Neill, B. C. et al. (2016). 'The Scenario Model Intercomparison Project (ScenarioMIP) for CMIP6'. eng. In: *Geoscientific model development* vol. 9, no. 9, pp. 3461–3482.

O'Neill, B. C. et al. (2017). 'The roads ahead: Narratives for shared socioeconomic pathways describing world futures in the 21st century'. eng. In: *Global environmental change* vol. 42, no. January, pp. 169–180.

Payne, A. J. et al. (2021). 'Future Sea Level Change Under Coupled Model Intercomparison Project Phase 5 and Phase 6 Scenarios From the Greenland and Antarctic Ice Sheets'. eng. In: *Geophysical research letters* vol. 48, no. 16, n/a.

Rummukainen, M. (2010). 'State-of-the-art with regional climate models'. eng. In: *Wiley interdisciplinary reviews. Climate change* vol. 1, no. 1, pp. 82–96.

Screen, J. A. and Simmonds, I. (2010). 'The central role of diminishing sea ice in recent Arctic temperature amplification'. eng. In: *Nature (London)* vol. 464, no. 7293, pp. 1334–1337.

Shupe, M. D. and Intrieri, J. M. (2004). 'Cloud Radiative Forcing of the Arctic Surface: The Influence of Cloud Properties, Surface Albedo, and Solar Zenith Angle'. eng. In: *Journal of climate* vol. 17, no. 3, pp. 616–628.

Tedesco, M. and Fettweis, X. (2020). 'Unprecedented atmospheric conditions (1948–2019) drive the 2019 exceptional melting season over the Greenland ice sheet'. In: *The Cryosphere* vol. 14, no. 4, pp. 1209–1223.

The IMBIE Team (2020). 'Mass balance of the Greenland Ice Sheet from 1992 to 2018'. eng. In: *Nature (London)* vol. 579, no. 7798, pp. 233–239.

van den Broeke, M., Smeets, P., Ettema, J., Van Der Veen, C., Van De Wal, R. and Oerlemans, J. (2008b). 'Partitioning of melt energy and meltwater fluxes in the ablation zone of the west Greenland ice sheet'. eng. In: *The cryosphere* vol. 2, no. 2, pp. 179–189.

van den Broeke, M., Enderlin, E., Howat, I., Kuipers Munneke, P., Noël, B., Jan Van De Berg, W., Van Meijgaard, E. and Wouters, B. (2016). 'On the recent contribution of the Greenland ice sheet to sea level change'. eng. In: *The cryosphere* vol. 10, no. 5, pp. 1933–1946.

van den Broeke, M., Bamber, J., Ettema, J., Rignot, E., Schrama, E., Berg, W. J. van de, Meijgaard, E. van, Velicogna, I. and Wouters, B. (2009). 'Partitioning Recent Greenland Mass Loss'. In: *Science* vol. 326, no. 5955, pp. 984–986.

van den Broeke, M., Box, J., Fettweis, X., Hanna, E., Noël, B., Tedesco, M., As, D. van, Berg, W. J. van de and Kampenhout, L. van (2017). 'Greenland Ice Sheet Surface Mass Loss: Recent Developments in Observation and Modeling'. eng. In: *Current climate change reports* vol. 3, no. 4, pp. 345–356.

Van Tricht, K., Lhermitte, S., Lenaerts, J. T. M., Gorodetskaya, I. V., L'Ecuyer, T. S., Noël, B., Van Den Broeke, M. R., Turner, D. D. and Van Lipzig, N. P. M. (2016). 'Clouds enhance Greenland ice sheet meltwater runoff'. eng. In: *Nature communications* vol. 7, no. 1, pp. 10266–10266.

Vionnet, V., Brun, E., Morin, S., Boone, A., Faroux, S., Le Moigne, P., Martin, E. and Willemet, J.-M. (2012). 'The detailed snowpack scheme Crocus and its implementation in SURFEX v7.2'. eng. In: *Geoscientific model development* vol. 5, no. 3, pp. 773–791.

WCRP, W. C. R. P. (2020). *WCRP Coupled Model Intercomparison Project (CMIP)*. URL: https://www.wcrp-climate.org/wgcm-cmip (visited on 22/12/2020).

Zelinka, M. D., Myers, T. A., McCoy, D. T., Po-Chedley, S., Caldwell, P. M., Ceppi, P., Klein, S. A. and Taylor, K. E. (2020). 'Causes of Higher Climate Sensitivity in CMIP6 Models'. eng. In: *Geophysical research letters* vol. 47, no. 1, n/a.